

# Sum of Squared Extended $\eta$ - $\mu$ and $\kappa$ - $\mu$ RVs: A New Framework Applied to FR3 and Sub-THz Systems

Gustavo Rodrigues de Lima Tejerina and Italo Atzeni

**Abstract**—The analysis of systems operating in future frequency ranges calls for a proper statistical channel characterization through generalized fading models. In this paper, we adopt the Extended  $\eta$ - $\mu$  and  $\kappa$ - $\mu$  models to characterize the propagation in FR3 and the sub-THz band, respectively. For these models, we develop a new exact representation of the sum of squared independent and identically distributed random variables, which can be used to express the power of the received signal in multi-antenna systems. Unlike existing ones, the proposed analytical framework is remarkably tractable and computationally efficient, and thus can be conveniently employed to analyze systems with massive antenna arrays. For both the Extended  $\eta$ - $\mu$  and  $\kappa$ - $\mu$  distributions, we derive novel expressions for the probability density function and cumulative distribution function, we analyze their convergence and truncation error, and we discuss the computational complexity and implementation aspects. Moreover, we derive expressions for the outage and coverage probability, bit error probability for coherent binary modulations, and symbol error probability for  $M$ -ary phase-shift keying and quadrature amplitude modulation. Lastly, we provide an extensive performance evaluation of FR3 and sub-THz systems focusing on a downlink scenario where a single-antenna user is served by a base station employing maximum ratio transmission.

**Index Terms**—Generalized fading models, Extended  $\eta$ - $\mu$  distribution,  $\kappa$ - $\mu$  distribution, FR3, sub-THz band.

## I. INTRODUCTION

Current fifth-generation (5G) wireless systems support operations in two frequency ranges: sub-6 GHz, referred to in the 3rd Generation Partnership Project (3GPP) as FR1 and recently expanded up to 7.125 GHz [1], and low millimeter-wave, referred to in 3GPP as FR2 and spanning from 24.25 to 71 GHz [2]. Future releases of 5G are expected to extend operations to the upper mid-band, referred to in 3GPP as FR3 and encompassing the 7.125–24.25 GHz range [3]. FR3 offers an attractive balance between bandwidth and coverage, and is characterized by mild propagation conditions compared with FR2 [4]. On the other hand, sixth-generation (6G) wireless systems are envisioned to explore the sub-THz spectrum, ranging from 100 to 300 GHz, to seek extreme bandwidths and accommodate an unprecedented number of users with high data rates [5]. In general, raising the carrier frequency has a two-fold impact on the propagation. First, the penetration loss and roughness of the materials with respect to the wavelength increase: consequently, the impact of the non-line-of-sight (NLoS) paths tends to diminish and the line-of-sight (LoS) component becomes dominant. Second, the free-space path

loss (for isotropic antennas) increases: thus, more antennas are needed to create physically large arrays that are capable of properly focusing the signal power. These properties are clearly exacerbated when moving up in frequency from FR3 to FR2 and then to the sub-THz band [6].

Wireless channels are generally modeled deterministically or statistically [7]. The deterministic approach captures the channel characteristics through site-specific measurements and simulations using, e.g., ray tracing and finite-difference time-domain. The statistical approach models the fluctuations of the channel through tractable probability distributions to incorporate, e.g., LoS, multipath, and scattering components. For example, the classical Rayleigh, Rice, and Nakagami- $m$  models are commonly used to characterize the fading in the sub-6 GHz range. The suitability of these classical fading models to represent millimeter-wave and sub-THz channels has also been studied [8]–[11]. However, such models fail to properly capture the intricacies of the propagation at high frequencies, which motivates investigating more generalized ones such as the (Extended)  $\eta$ - $\mu$ ,  $\kappa$ - $\mu$ ,  $\alpha$ - $\mu$ ,  $\alpha$ - $\eta$ - $\kappa$ - $\mu$ , and fluctuating two-ray (FTR) models. For instance, [12] compared both classical and generalized fading models to measured data at 26, 28, and 39 GHz in LoS and NLoS scenarios, showing a better fit for the generalized models, i.e.  $\eta$ - $\mu$ ,  $\kappa$ - $\mu$ ,  $\alpha$ - $\mu$ , and  $\alpha$ - $\eta$ - $\kappa$ - $\mu$ . Similarly, [13] showed a better goodness of fit for the  $\alpha$ - $\mu$  model compared with classical models at 143.1 GHz by conducting field trials in both LoS and NLoS conditions in three different indoor environments. Furthermore, [14], [15] used measurements to demonstrate the aptness of the FTR and multi-cluster FTR distributions to model the fading at 143.1 GHz. Other works investigated generalized fading models applied to specific scenarios including, e.g., multiple antennas [16], reflective surfaces [14], [17], [18], dual-hop communications [19], and random atmospheric absorption [20].

Statistical channel characterization is constantly evolving to encompass new propagation environments. However, as more intricate scenarios arise, the mathematical complexity of the resulting models increases considerably. For example, when adding multiple antennas or reflective surfaces in the system, expressing the power of the received signal involves the sum or product of random variables (RVs), which greatly complicates the analysis. When successful, these representations are likely to employ elaborate special functions, such as Horn functions and the Fox H-function, as proposed for the Extended  $\eta$ - $\mu$  and  $\kappa$ - $\mu$  models applied to systems with maximum ratio combining (MRC) [21], [22] and pre-detection equal gain combining (EGC) [23] at the receiver. However, their widespread use is limited since these special functions are not readily available in

This work was supported by the Research Council of Finland (336449 Profi6, 348396 HIGH-6G, and 369116 6G Flagship) and by the European Commission (101095759 Hexa-X-II).

The authors are with the Centre for Wireless Communications, University of Oulu, Finland (e-mail: {gustavo.tejerina, italo.atzeni}@oulu.fi).

common mathematical packages such as MATLAB, Mathematica, and SciPy. To bypass this issue, researchers have resorted to simplified versions of classical and generalized fading models, namely Nakagami- $m$ , Extended  $\eta$ - $\mu$ , and  $\kappa$ - $\mu$ , where integer values are assumed for some of the parameters [24]–[26]. More recently, [27] developed an analytical framework based on complex analysis to represent the exact sum of independent and identically distributed (i.i.d.)  $\kappa$ - $\mu$  RVs. This framework leads to more tractable and computationally efficient expressions (i.e., given in terms of simple Gamma functions) for the probability density function (PDF) and cumulative distribution function (CDF). These results were exploited to derive expressions for the outage probability and bit error probability (BEP) with pre-detection EGC that also inherit the framework's simplicity. Following a similar approach, [28] represented the exact sum of i.i.d.  $\alpha$ - $\mu$  RVs and obtained the PDF and CDF for systems with MRC and pre-detection EGC at the receiver.

#### A. Contribution

The analysis of systems operating in future frequency ranges, from FR3 to the sub-THz band, is of paramount importance and calls for a proper statistical channel characterization through generalized fading models. In this paper, we adopt the Extended  $\eta$ - $\mu$  and  $\kappa$ - $\mu$  models to characterize the propagation in FR3 and the sub-THz band, respectively. Indeed, the Extended  $\eta$ - $\mu$  and  $\kappa$ - $\mu$  models provide remarkable flexibility to represent scenarios with dominant NLoS and LoS components, respectively, which well fit the propagation in FR3 and at sub-THz frequencies, respectively. In multi-antenna systems with maximum ratio transmission (MRT) at the transmitter or MRC at the receiver, the power of the received signal can be expressed as a sum of squared RVs. In this regard, [21] and [29] proposed expressions for the PDF and CDF of the sum of squared i.i.d. Extended  $\eta$ - $\mu$  and  $\kappa$ - $\mu$  RVs that employ special functions such as the Horn functions, modified Bessel function, and Marcum Q-function. More importantly, the evaluation of the performance metrics based on these expressions either involves the Fox-H function [21] and Horn functions [22], or requires cumbersome numerical integration. Thus, when raising the carrier frequency, existing analytical frameworks for the considered models become unsuitable to handle massive numbers of antennas due to their inherent computational complexity. To address this issue, we extend the framework in [27] and develop a new exact representation of the sum of squared i.i.d. Extended  $\eta$ - $\mu$  and  $\kappa$ - $\mu$  RVs. The resulting framework is remarkably tractable and computationally efficient, and thus can be conveniently employed to analyze FR3 and sub-THz systems with massive antenna arrays.

The contribution of this paper is summarized as follows.

- For both the Extended  $\eta$ - $\mu$  and  $\kappa$ - $\mu$  distributions, we build on the framework based on complex analysis in [27] to derive novel expressions for the PDF and CDF of the sum of squared i.i.d. RVs. The resulting expressions are given in terms of simple Gamma function, which makes them tractable and computationally efficient. Although these expressions include an infinite summation, they can be conveniently truncated with negligible errors even for a limited number of terms. In this context, we analyze

the convergence and truncation error. Furthermore, we discuss the computational complexity and implementation aspects.

- Based on the above expressions for the PDF and CDF, we derive expressions for important performance metrics such as the outage and coverage probability, BEP for coherent binary modulations, and symbol error probability (SEP) for  $M$ -ary phase-shift keying ( $M$ -PSK) and  $M$ -ary quadrature amplitude modulation ( $M$ -QAM), along with their asymptotic expressions at high signal-to-noise ratio (SNR). In this regard, we provide two distinct approaches with different computational complexities and convergence conditions. The obtained expressions are easy to evaluate numerically and reduce the computation time compared with the solutions in [21], [22].
- We provide an extensive performance evaluation of FR3 and sub-THz systems under the Extended  $\eta$ - $\mu$  and  $\kappa$ - $\mu$  models, respectively. In this regard, we focus on a downlink system where a single-antenna user is served by a multi-antenna base station (BS) employing MRT, with perfect and imperfect channel state information (CSI) at the latter. The evaluation is carried out in terms of distance between the BS and the user, number of antennas, transmit power, carrier frequency, fading parameters, and modulation order. For example, we observe that an eight-fold increase in the number of antennas enables the carrier frequency to be approximately doubled. Moreover, even in high-frequencies, LoS-dominated scenarios, the NLoS components continue to make a noticeable contribution to the received signal. Lastly, the LoS or NLoS path loss exponent has a greater impact than the frequency-dependent path loss factor.

**Outline.** The rest of the paper is structured as follows. Section II introduces the new representation of the sum of squared i.i.d. Extended  $\eta$ - $\mu$  and  $\kappa$ - $\mu$  RVs, presenting novel expressions for the PDF and CDF. Section III builds on the proposed framework to derive new expressions for the outage and coverage probability, BEP, and SEP. Section IV provides an extensive performance evaluation of FR3 and sub-THz systems. Lastly, Section V concludes the paper.

**Notation.** Boldface lowercase letters indicate vectors,  $\|\cdot\|$  is the euclidean norm, and  $(\cdot)^H$  is the Hermitian transpose operator.  $\mathbb{R}$  and  $\mathbb{C}$  indicate the sets of real and complex numbers, respectively, with  $j = \sqrt{-1}$ .  $\mathbb{E}[\cdot]$  is the expectation operator.  $f_X(x)$ ,  $F_X(x)$ , and  $\mathcal{M}_X(s)$  correspond to the PDF, CDF, and moment-generating function (MGF), respectively, of RV  $X$ .  $\text{erfc}(\cdot)$  denotes the complementary error function [30, Eq. (06.27.07.0001.01)],  $\Gamma(\cdot)$  is the Gamma function [30, Eq. (06.05.02.0001.01)],  $\Gamma(\cdot, \cdot)$  is the incomplete Gamma function [30, Eq. (06.06.02.0001.01)], and  $B(\cdot, \cdot, \cdot)$  indicates the incomplete Beta function [30, Eq. (06.19.02.0001.01)].  $I_\nu(\cdot)$  is the modified Bessel function of the first kind and  $\nu$ -th order [30, Eq. (03.02.02.0001.01)].  ${}_1F_1(\cdot; \cdot; \cdot)$  is the Kummer confluent hypergeometric function [30, Eq. (07.20.02.0001.01)].  ${}_2F_1(\cdot, \cdot; \cdot; z)$  for  $|z| < 1$  denotes the Gauss hypergeometric function [30, Eq. (07.23.02.0001.01)].  ${}_pF_q(a_1, \dots, a_p; b_1, \dots, b_q; z)$  is the generalized hypergeomet-

ric function [30, Eq. (07.31.02.0001.01)] for  $|z| < 1$  if  $q = p - 1$  or  $\forall z \in \mathbb{R}$  if  $q \geq p$ .  $F_1(\cdot; \cdot, \cdot; \cdot; z_1, z_2)$  for  $|z_1| < 1$  and  $|z_2| < 1$  is the Appell hypergeometric function [30, Eq. (07.36.02.0001.01)]. Lastly,  $\sim$  means asymptotically equivalent.

## II. SUM OF SQUARED RVs: NEW FRAMEWORK

Considering a multi-antenna BS serving a single-antenna user, the sum of squared RVs can be used to express the instantaneous uplink SNR when the BS adopts MRC or post-detection EGC, or the instantaneous downlink SNR when the BS adopts MRT. In this paper, we focus on the latter as our motivating scenario and for our performance evaluation, although the proposed analytical framework also applies to the other settings.

In this context, consider a BS equipped with  $N$  antennas transmitting data to a single-antenna user. The signal received at the user is given by

$$y = \sqrt{P_t} \mathbf{g}^H \mathbf{v} x + z \in \mathbb{C}, \quad (1)$$

where  $P_t$  is the transmit power,  $\mathbf{g} = [g_1, \dots, g_N] \in \mathbb{C}^N$  is the channel vector,  $\mathbf{v} \in \mathbb{C}^N$  is the precoding vector (with  $\|\mathbf{v}\|^2 = 1$ ),  $x \in \mathbb{C}$  is the transmitted data symbol (with  $\mathbb{E}[|x|^2] = 1$ ), and  $z \sim \mathcal{CN}(0, \sigma^2)$  is the noise term. With perfect CSI, the MRT precoding vector is given by  $\mathbf{v} = \mathbf{g}/\|\mathbf{g}\|$  and the corresponding instantaneous SNR at the user is

$$\text{SNR}_p = \frac{P_t}{\sigma^2} |\mathbf{g}^H \mathbf{v}|^2 = \frac{P_t}{\sigma^2} \sum_{n=1}^N |g_n|^2. \quad (2)$$

Alternatively, assuming a simplified model for imperfect CSI, the MRT precoding vector is given by  $\mathbf{v} = \hat{\mathbf{g}}/\|\hat{\mathbf{g}}\|$ , where  $\hat{\mathbf{g}} = \sqrt{1 - \alpha^2} \mathbf{g} + \alpha \hat{\mathbf{g}} \in \mathbb{C}^N$  denotes the estimated channel,  $\hat{\mathbf{g}} \sim \mathcal{CN}(\mathbf{0}, \frac{1}{N} \|\mathbf{g}\|^2 \mathbf{I}_N)$  is the channel estimation error (independent of  $\mathbf{g}$ ), and  $\alpha \in [0, 1]$  is the estimation accuracy (with  $\alpha = 0$  representing perfect CSI). When  $N \gg 1$ , the corresponding instantaneous SNR at the user can be approximated as

$$\text{SNR}_I \simeq (1 - \alpha^2) \text{SNR}_p, \quad (3)$$

with  $\text{SNR}_p$  defined in (2). Note that (2) and (3) can also be used to characterize the instantaneous uplink SNR when the BS adopts MRC.

Motivated by the above system model, we propose a new exact representation of the sum of squared i.i.d. Extended  $\eta$ - $\mu$  and  $\kappa$ - $\mu$  RVs. The proposed framework is based on the recursive solution provided in [27] and results in much simpler expressions for the PDF and CDF (i.e., given in terms of simple Gamma functions) compared with [21], [22], [29], which employed special functions such as the modified Bessel function, Marcum Q-function, and Horn functions. Hence, the resulting performance metrics, such as the BEP and SEP, also inherit the framework's simplicity. Furthermore, we analyze the convergence, truncation error, and computational complexity of these new expressions. The proposed framework has proven to return fast and precise solutions even when employing a very large number of antennas. In the rest of this section (as well as in Section III), we present all the detailed steps for the Extended  $\eta$ - $\mu$  distribution and only a sketch of the procedure for the  $\kappa$ - $\mu$  distribution, which follows the same rationale.

### A. PDF and CDF for the Extended $\eta$ - $\mu$ Distribution

The Extended  $\eta$ - $\mu$  model is a generalized fading model used to represent scenarios with dominant NLoS components with power and cluster imbalances [31]. These features are enabled through the parameters  $\eta$ ,  $\mu$ , and  $p$ , where  $\eta > 0$  denotes the power ratio between the in-phase and quadrature signals,  $\mu > 0$  is the number of multipath clusters, and  $p > 0$  represents the ratio between the numbers of multipath clusters of the in-phase and of the quadrature components. The Extended  $\eta$ - $\mu$  model is known to encompass classical fading models such as Hoyt, Nakagami- $m$ , and Rayleigh. For the Extended  $\eta$ - $\mu$  distribution, the PDF of the envelope of the  $n$ -th RV, denoted by  $R_n = \sqrt{\frac{P_t}{\sigma^2}} |g_n|$ , is defined as [31, Eq. (14)]

$$f_{R_n}(r_n) = \frac{2\xi^\mu r_n^{2\mu-1} {}_1F_1\left(\frac{\mu p}{1+p}; \mu; \frac{\xi(\eta-p)r_n^2}{\eta \hat{w}_n}\right)}{\Gamma(\mu) \hat{w}_n^\mu \exp\left(\xi \frac{r_n^2}{\hat{w}_n}\right)} \left(\frac{p}{\eta}\right)^{\frac{\mu p}{1+p}}, \quad (4)$$

with  $\xi = \mu(1 + \eta)/(1 + p)$ , and where  $\hat{w}_n = \mathbb{E}[R_n^2]$  represents the expectation of the squared envelope of the  $n$ -th RV. For the new representation of the sum of  $N$  squared i.i.d. RVs, we follow the standard MGF-based approach to obtain the PDF. This procedure consists in first deriving the MGF of a transformed RV (i.e., the square of the original RV) and then expressing the sum as the product of  $N$  MGFs.

For the first step, we begin by applying the RV transformation  $W_n = R_n^2 = \frac{P_t}{\sigma^2} |g_n|^2$  in (4), resulting in

$$f_{W_n}(w_n) = \frac{\xi^\mu w_n^{\mu-1} {}_1F_1\left(\frac{\mu p}{1+p}; \mu; \frac{\xi(\eta-p)w_n}{\eta \hat{w}_n}\right)}{\Gamma(\mu) \hat{w}_n^\mu \exp\left(\xi \frac{w_n}{\hat{w}_n}\right)} \left(\frac{p}{\eta}\right)^{\frac{\mu p}{1+p}}. \quad (5)$$

Then, the MGF of (5) is obtained after applying the Laplace transform, i.e.,  $\mathcal{M}_X(s) = \int_0^\infty f_X(x) \exp(-sx) dx$ , leading to

$$\begin{aligned} \mathcal{M}_{W_n}(s) &= \frac{\xi^\mu}{\Gamma(\mu) \hat{w}_n^\mu} \left(\frac{p}{\eta}\right)^{\frac{\mu p}{1+p}} \int_0^\infty \frac{w_n^{\mu-1}}{\exp(s w_n + \frac{\xi w_n}{\hat{w}_n})} \\ &\quad \times {}_1F_1\left(\frac{\mu p}{1+p}; \mu; \frac{\xi(\eta-p)w_n}{\eta \hat{w}_n}\right) dw_n. \end{aligned} \quad (6)$$

Following the same rationale of [27], we rewrite the exponential function and Kummer confluent hypergeometric function  ${}_1F_1$  according to their contour integral representations [30, Eq. (07.20.07.0003.01), (01.03.07.0001.01)], which results in

$$\begin{aligned} \mathcal{M}_{W_n}(s) &= \frac{\xi^\mu \left(\frac{p}{\eta}\right)^{\frac{\mu p}{1+p}}}{(2\pi j)^2 \Gamma\left(\frac{\mu p}{1+p}\right)} \int_0^\infty \oint_{\mathcal{L}_t} \oint_{\mathcal{L}_v} \frac{\Gamma(t) \Gamma(v) \left(\frac{\eta \xi}{p-\eta}\right)^v}{\Gamma(\mu - v)} \\ &\quad \times \frac{\Gamma\left(\frac{\mu p}{1+p} - v\right) w_n^{\mu-t-v-1}}{\exp\left(\frac{\xi w_n}{\hat{w}_n}\right) s^t \hat{w}_n^{\mu-v}} dv dt dw_n, \end{aligned} \quad (7)$$

where  $\mathcal{L}_t$  and  $\mathcal{L}_v$  are the complex contours of  $t$  and  $v$ , respectively. After this procedure, the integral operators in (7) are reordered to solve it in terms of  $w_n$ , leading to

$$\begin{aligned} \mathcal{M}_{W_n}(s) &= \frac{(2\pi j)^{-2}}{\Gamma\left(\frac{\mu p}{1+p}\right)} \left(\frac{p}{\eta}\right)^{\frac{\mu p}{1+p}} \oint_{\mathcal{L}_t^*} \oint_{\mathcal{L}_v^*} \frac{\Gamma(t) \Gamma(v)}{\Gamma(\mu - v)} \\ &\quad \times \frac{\Gamma(\mu - t - v) \Gamma\left(\frac{\mu p}{1+p} - v\right)}{\left(\frac{p}{\eta} - 1\right)^v \left(\frac{\xi}{s \hat{w}_n}\right)^{-t}} dv dt, \end{aligned} \quad (8)$$

where  $\mathcal{L}_t^*$  and  $\mathcal{L}_v^*$  are the new complex contours of  $t$  and  $v$ , respectively, after the integration over  $w_n$ . With this procedure, (8) has new essential singularities located at  $t \in \{-m, (l -$

$m + \mu\}$  and at  $v \in \{l + \mu p / (1 + p), l + \mu, -l\}$ . As in [27], by identifying the singularities, the new complex contours are defined to guarantee the convergence of (8) and circumvent duplicate poles. With this in mind, both contour integrals can be solved by applying the residue theorem [32, Eq. (16.3.6)] to (8) for the poles  $t \rightarrow m - l + \mu$  and  $v \rightarrow -l$ , obtaining

$$\mathcal{M}_{W_n}(s) = \frac{\left(\frac{p}{\eta}\right)^{\frac{\mu p}{1+p}}}{\Gamma\left(\frac{\mu p}{1+p}\right)} \sum_{m=0}^{\infty} \sum_{l=0}^{\infty} \left(\frac{p}{\eta} - 1\right)^l \left(\frac{\xi}{s\hat{w}_n}\right)^{l+m+\mu} \times \frac{\Gamma(l+m+\mu)\Gamma\left(l+\frac{\mu p}{1+p}\right)}{(-1)^m(-1)^l m! l! \Gamma(l+\mu)}. \quad (9)$$

Finally, (9) is rearranged in terms of Cauchy product as

$$\mathcal{M}_{W_n}(s) = \frac{\left(\frac{p}{\eta}\right)^{\frac{\mu p}{1+p}} \left(\frac{\xi}{s\hat{w}_n}\right)^{\mu}}{\Gamma\left(\frac{\mu p}{1+p}\right)} \sum_{m=0}^{\infty} \left(-\frac{\xi}{s\hat{w}_n}\right)^m \sum_{l=0}^m \frac{\Gamma(\mu+m)}{(m-l)!} \times \frac{\Gamma(-l+m+\frac{\mu p}{1+p}) \left(\frac{p}{\eta} - 1\right)^{m-l}}{l! \Gamma(-l+m+\mu)}. \quad (10)$$

For the second step, the MGF of the sum of  $N$  i.i.d. RVs  $W_n$ , denoted by  $W = \sum_{n=1}^N W_n = \text{SNR}_p$ , is obtained as the product of their respective MGFs, i.e.,  $\mathcal{M}_W(s) = \prod_{n=1}^N \mathcal{M}_{W_n}(s)$ . Hence, from (10) and [33, Eq. (0.314)], the product of the MGFs is given by

$$\mathcal{M}_W(s) = \left(\frac{\xi^{\mu} \left(\frac{p}{\eta}\right)^{\frac{\mu p}{1+p}}}{\Gamma\left(\frac{\mu p}{1+p}\right)}\right)^N \sum_{m=0}^{\infty} \left(\frac{1}{s\hat{w}}\right)^{N\mu+m} h_m, \quad (11)$$

where we have replaced  $\hat{w}_n = \hat{w}$ ,  $\forall n$  due to the i.i.d. property and with

$$h_0 = \Gamma\left(\frac{\mu p}{1+p}\right)^N, \quad (12a)$$

$$h_m = \sum_{i=1}^m \frac{(iN+i-m)h_{m-i}}{m\Gamma\left(\frac{\mu p}{1+p}\right)(-\xi)^{-i}} \sum_{l=0}^i \frac{\Gamma(i+\mu)}{l!(i-l)!} \times \frac{\Gamma(i-l+\frac{\mu p}{1+p}) \left(\frac{p}{\eta} - 1\right)^{i-l}}{\Gamma(i-l+\mu)}, \quad m \geq 1. \quad (12b)$$

Finally, the inverse Laplace transform is applied to (11) by using [33, Eq. (17.13.3)] and the PDF is obtained as

$$f_W(w) = \left(\frac{\left(\frac{p}{\eta}\right)^{\frac{\mu p}{1+p}} \xi^{\mu}}{\Gamma\left(\frac{\mu p}{1+p}\right)}\right)^N \sum_{m=0}^{\infty} \frac{w^{N\mu+m-1} h_m}{\hat{w}^{N\mu+m} \Gamma(N\mu+m)}, \quad (13)$$

with  $h_m$  defined in (12). The CDF readily follows from applying the standard procedure, i.e.,  $F_X(x) = \int_0^x f_X(x) dx$ , which yields

$$F_W(w) = \left(\frac{\left(\frac{p}{\eta}\right)^{\frac{\mu p}{1+p}} \xi^{\mu}}{\Gamma\left(\frac{\mu p}{1+p}\right)}\right)^N \sum_{m=0}^{\infty} \frac{\left(\frac{w}{\hat{w}}\right)^{m+\mu N} h_m}{\Gamma(N\mu+m+1)}. \quad (14)$$

An alternative MGF representation can be obtained from (9) by simplifying its  $m$ -indexed summation and reducing it to a power function, leading to

$$\mathcal{M}_{W_n}(s) = \frac{\left(\frac{p}{\eta}\right)^{\frac{\mu p}{1+p}}}{\Gamma\left(\frac{\mu p}{1+p}\right)} \sum_{l=0}^{\infty} \frac{(1-\frac{p}{\eta})^l \Gamma\left(l+\frac{\mu p}{1+p}\right)}{\Gamma(l+1)} \left(\frac{1}{1+\frac{s\hat{w}}{\xi}}\right)^{l+\mu}. \quad (15)$$

After rearranging (15) and with the help of [33, Eq. (0.314)],

we obtain the reformulated MGF as (cf. (11))

$$\mathcal{M}_W(s) = \left(\frac{\left(\frac{p}{\eta}\right)^{\frac{\mu p}{1+p}}}{\Gamma\left(\frac{\mu p}{1+p}\right)}\right)^N \sum_{m=0}^{\infty} \left(\frac{1}{1+\frac{s\hat{w}}{\xi}}\right)^{N\mu+m} \tilde{h}_m, \quad (16)$$

with (cf. (12))

$$\tilde{h}_0 = \Gamma\left(\frac{\mu p}{1+p}\right)^N, \quad (17a)$$

$$\tilde{h}_m = \frac{1}{m\Gamma\left(\frac{\mu p}{1+p}\right)} \sum_{k=1}^m (kN+k-m) \tilde{h}_{m-k} \times \frac{(1-\frac{p}{\eta})^k \Gamma\left(k+\frac{\mu p}{1+p}\right)}{\Gamma(k+1)}, \quad m \geq 1. \quad (17b)$$

From (16), the PDF is obtained as (cf. (13))

$$f_W(w) = \left(\frac{\left(\frac{p}{\eta}\right)^{\frac{\mu p}{1+p}}}{\Gamma\left(\frac{\mu p}{1+p}\right)}\right)^N \sum_{m=0}^{\infty} \frac{\left(\frac{\xi w}{\hat{w}}\right)^{N\mu+m} \tilde{h}_m}{w \Gamma(N\mu+m) \exp\left(\frac{\xi w}{\hat{w}}\right)}, \quad (18)$$

whereas the CDF is given by (cf. (14))

$$F_W(w) = \left(\frac{\left(\frac{p}{\eta}\right)^{\frac{\mu p}{1+p}}}{\Gamma\left(\frac{\mu p}{1+p}\right)}\right)^N \sum_{m=0}^{\infty} \left(1 - \frac{\Gamma(N\mu+m, \frac{\xi w}{\hat{w}})}{\Gamma(N\mu+m)}\right) \tilde{h}_m. \quad (19)$$

In Section III, we will use the PDFs in (13) and (18) (resp. the MGFs in (11) and (16)) to derive two distinct sets of expressions for the BEP (resp. SEP): one with lower computational complexity but quite restrictive convergence conditions, and another with slightly higher computational complexity and no restrictions on the convergence. The same applies to the PDFs in (23) and (27) (resp. MGFs in (21) and (25)) presented in the next section for the  $\kappa$ - $\mu$  distribution.

### B. PDF and CDF for the $\kappa$ - $\mu$ Distribution

The  $\kappa$ - $\mu$  model is a generalized fading model used to represent scenarios with a dominant LoS component [34]. This feature is enabled through the parameters  $\kappa$  and  $\mu$ , where  $\kappa > 0$  represents the power ratio between the LoS and NLoS (i.e., scattered) components and  $\mu > 0$  indicates the number of multipath clusters (as in the Extended  $\eta$ - $\mu$  model). The  $\kappa$ - $\mu$  model is known to encompass classical fading models such as Nakagami- $m$ , Rice, and Rayleigh. For the  $\kappa$ - $\mu$  distribution, the PDF of the envelope of the  $n$ -th RV is defined as [34, Eq. (1)]

$$f_{R_n}(r_n) = \frac{2\mu(\kappa+1)^{\frac{\mu+1}{2}} r_n^{\mu} I_{\mu-1}(2\mu\sqrt{\kappa(\kappa+1)}\frac{r_n^2}{\hat{w}_n})}{\kappa^{\frac{\mu-1}{2}} \hat{w}_n^{\frac{\mu+1}{2}} \exp(\kappa\mu + (\kappa+1)\mu\frac{r_n^2}{\hat{w}_n})}. \quad (20)$$

For the new representation of the sum of  $N$  squared i.i.d.  $\kappa$ - $\mu$  RVs, we follow similar steps as for the Extended  $\eta$ - $\mu$  distribution.

For the first step, we begin by applying the RV transformation  $W_n = R_n^2$ . Then, we apply the Laplace transform and use the contour representations of the exponential and Bessel functions [30, Eq. (03.02.07.0009.01)]. Furthermore, the contour integrals are solved for the poles  $t \rightarrow \frac{1}{2}(\mu+2m-2v+1)$  and  $v \rightarrow \frac{1}{2}(-2l-\mu+1)$ , which results in the MGF of  $W_n$ . For the second step, we obtain the product of the MGFs as

$$\mathcal{M}_W(s) = \left(\frac{(\kappa+1)\mu}{\exp(\kappa)}\right)^{N\mu} \sum_{m=0}^{\infty} \left(\frac{1}{s\hat{w}}\right)^{N\mu+m} k_m, \quad (21)$$

with

$$k_0 = 1, \quad (22a)$$

$$k_m = \frac{1}{m} \sum_{i=1}^m (i - m + Ni) \Gamma(i + \mu) k_{m-i} \times \sum_{l=0}^i \frac{(-\kappa\mu)^{-l} (\kappa(\kappa + 1)\mu^2)^i}{l!(i-l)!\Gamma(-l + i + \mu)}, \quad m \geq 1. \quad (22b)$$

Finally, the inverse Laplace transform is applied to (21) and the PDF is obtained as

$$f_W(w) = \left( \frac{(\kappa + 1)\mu}{\exp(\kappa)} \right)^{N\mu} \sum_{m=0}^{\infty} \frac{w^{N\mu+m-1} k_m}{\hat{w}^{N\mu+m} \Gamma(N\mu + m)}, \quad (23)$$

with  $k_m$  defined in (22). The CDF readily follows as

$$F_W(w) = \left( \frac{(\kappa + 1)\mu}{\exp(\kappa)} \right)^{N\mu} \sum_{m=0}^{\infty} \frac{\left( \frac{w}{\hat{w}} \right)^{N\mu+m} k_m}{\Gamma(N\mu + m + 1)}. \quad (24)$$

An alternative MGF representation can be obtained as (cf. (21))

$$\mathcal{M}_W(s) = \sum_{m=0}^{\infty} \frac{\tilde{k}_m}{\exp(N\kappa\mu)} \left( \frac{K}{K + s\hat{w}} \right)^{N\mu+m}, \quad (25)$$

with (cf. (22))

$$\tilde{k}_0 = 1, \quad (26a)$$

$$\tilde{k}_m = \frac{1}{m} \sum_{i=1}^m \frac{(Ni + i - m)(\kappa\mu)^i \tilde{k}_{m-i}}{\Gamma(i + 1)}, \quad m \geq 1. \quad (26b)$$

From (25), the PDF is obtained as (cf. (23))

$$f_W(w) = \frac{\exp\left(-\frac{Kw}{\hat{w}}\right)}{\exp(N\kappa\mu)} \sum_{m=0}^{\infty} \frac{\left(\frac{Kw}{\hat{w}}\right)^{N\mu+m} \tilde{k}_m}{w\Gamma(N\mu + m)}, \quad (27)$$

whereas the CDF is given by (cf. (24))

$$F_W(w) = \sum_{m=0}^{\infty} \left( 1 - \frac{\Gamma(N\mu + m, \frac{Kw}{\hat{w}})}{\Gamma(N\mu + m)} \right) \frac{\tilde{k}_m}{\exp(N\kappa\mu)}. \quad (28)$$

### C. Convergence and Truncation Analysis

In this section, we analyze the convergence of the infinite summations in (13)–(14) and (23)–(24). In calculus, the convergence of a numerical series is commonly inferred through its absolute convergence, which occurs when the sum of the absolute values of the individual terms converges [33, Eq. (0.21)]. Hence, we prove the absolute convergence by obtaining an upper bound on the summations in (13)–(14) and (23)–(24), as done in [27]. With this outcome, we derive the truncation error associated with the PDF and CDF of each distribution, which provides useful insights into the number of terms needed to numerically compute these functions with the desired accuracy.

For the summations in (13)–(14) of the Extended  $\eta$ - $\mu$  distribution, we need to ensure that the inequality

$$\mathcal{C}_\eta = \sum_{m=0}^{\infty} \frac{w^{N\mu+m-1+\zeta}}{\hat{w}^{N\mu+m} \Gamma(N\mu + m + \zeta)} |h_m| < \infty \quad (29)$$

holds, where  $\zeta = 0$  and  $\zeta = 1$  correspond to (13) and (14), respectively. To this end, we first upper bound  $|h_m|$  for  $m \geq 1$

as

$$|h_m| < \frac{1}{m\Gamma\left(\frac{\mu p}{1+p}\right)} \sum_{i=1}^m (Ni + i - m) \Gamma(i + \mu) \xi^i |h_{m-i}| \times \sum_{l=0}^i \frac{\Gamma(i - l + \frac{\mu p}{1+p})}{l!(i-l)!\Gamma(i - l + \mu)} \left( \frac{p}{\eta} - 1 \right)^{i-l}. \quad (30)$$

Since  $\Gamma(i - l + \mu p / (1 + p)) / \Gamma(i - l + \mu) \leq \Gamma(\mu p / (1 + p)) / \Gamma(\mu)$  and  $1 / \Gamma(\mu) < 8 / 7$  for any choice of  $\mu$  and  $p$ , we can upper bound the  $l$ -indexed summation in (30) by a power function [33, Eq. (1.111)], leading to

$$|h_m| < \frac{8}{7m} \sum_{i=1}^m \frac{(Ni + i - m) \Gamma(i + \mu) |h_{m-i}|}{\Gamma(i + 1) \left( \frac{\xi p}{\eta} \right)^{-i}}. \quad (31)$$

Considering the last term of the summation (corresponding to  $i = m$ ) and the fact that  $1 / \Gamma(m + 1) < 1 / \Gamma(m)$ , we obtain the simpler upper bound

$$|h_m| < \frac{8N\Gamma(m + \mu)}{7\Gamma(m)} \left( \xi \frac{p}{\eta} \right)^m |h_0|. \quad (32)$$

Now, we extend (32) to all  $m$  by substituting the right-hand side of (32) into (29) and performing the index change  $m = k + 1$ . After some mathematical manipulations, we obtain the following upper bound on (29):

$$\mathcal{C}_\eta < \frac{w^{N\mu-1+\zeta} |h_0|}{\hat{w}^{N\mu} \Gamma(N\mu + \zeta)} \left( 1 + \frac{8N\Gamma(N\mu + \zeta) \Gamma(\mu + 1)}{7\Gamma(N\mu + 1 + \zeta)} \times \frac{w\xi p}{\hat{w}\eta} {}_1F_1\left(\mu + 1; N\mu + 1 + \zeta; \frac{w\xi p}{\hat{w}\eta}\right) \right). \quad (33)$$

Finally, the absolute convergence of (29) and, consequently, the convergence of (13)–(14), follows from observing that the Kummer confluent hypergeometric function  ${}_1F_1$  in (33) is finite for any choice of parameters in our framework.

Furthermore, we derive an upper bound on the truncation error when applied to (13)–(14). We begin by defining the truncation error as the sum of the truncated terms, i.e.,

$$\mathcal{E}_\eta(\epsilon) = \left( \frac{\left( \frac{p}{\eta} \right)^{\frac{\mu p}{1+p}} \xi^\mu}{\Gamma\left(\frac{\mu p}{1+p}\right)} \right)^N \sum_{m=\epsilon}^{\infty} \frac{\left( \frac{w}{\hat{w}} \right)^{N\mu+m} h_m}{w^{1-\zeta} \Gamma(N\mu + m + \zeta)}, \quad (34)$$

where  $\epsilon$  indicates the number of terms employed to evaluate (13)–(14). From (34), we follow similar steps as those leading to (33) and, after some mathematical manipulations, we obtain the upper bound

$$\mathcal{E}_\eta(\epsilon) < \frac{8N\Gamma(\mu + \epsilon) \xi^{N\mu+\epsilon} w^{N\mu+\epsilon-1+\zeta}}{7\Gamma(\epsilon) \Gamma(N\mu + \epsilon + \zeta) \hat{w}^{N\mu+\epsilon}} \left( \frac{p}{\eta} \right)^{\frac{N\mu p}{1+p} + \epsilon} \times {}_2F_2\left(1, \mu + \epsilon; N\mu + \epsilon + \zeta, \epsilon; \frac{\xi p w}{\eta \hat{w}}\right). \quad (35)$$

For the summations in (23)–(24) of the  $\kappa$ - $\mu$  distribution, we follow similar steps as for the summations in (13)–(14) of the Extended  $\eta$ - $\mu$  distribution. Hence, we obtain the upper bound

$$\mathcal{C}_\kappa < \frac{w^{N\mu-1+\zeta}}{\hat{w}^{N\mu} \Gamma(N\mu + \zeta)} \left( 1 + \frac{8N\Gamma(\mu + 1) \Gamma(N\mu + \zeta) w}{7\Gamma(N\mu + 1 + \zeta) \hat{w}} \times K {}_1F_1\left(\mu + 1; N\mu + 1 + \zeta; \frac{Kw}{\hat{w}}\right) \right), \quad (36)$$

with  $K = \mu(\kappa + 1)(\kappa\mu + 1)$ , and where  $\zeta = 0$  and  $\zeta = 1$  correspond to (23) and (24), respectively. Again, the absolute convergence of (23)–(24) follows from observing that the

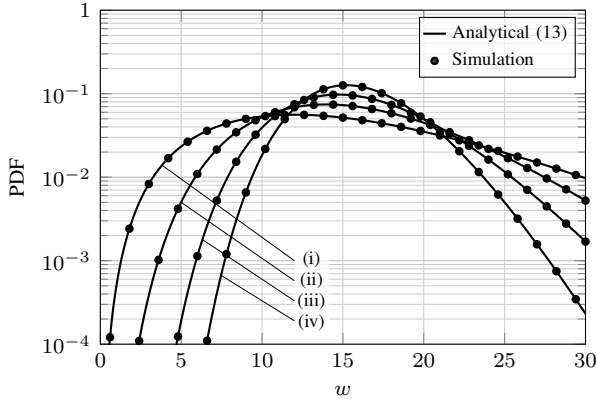


Fig. 1. PDF of the sum of squared i.i.d. Extended  $\eta$ - $\mu$  RVs, with  $N = 16$ ,  $\hat{w} = 1$ , and the following combinations of parameters: (i)  $\eta \rightarrow 0$ ,  $\mu = 0.5$ ,  $p = 1$  (Nakagami- $m$ ); (ii)  $\eta = 0.6$ ,  $\mu = 0.5$ ,  $p = 0.5$ ; (iii)  $\eta = 0.25$ ,  $\mu = 1.25$ ,  $p = 1.1$ , and (iv)  $\eta = 1.5$ ,  $\mu = 2$ ,  $p = 0.5$ .

Kummer confluent hypergeometric function  ${}_1F_1$  in (36) is finite for any choice of parameters in our framework. Moreover, we obtain the upper bound on the truncation error as

$$\mathcal{E}_\kappa(\epsilon) < \left( \frac{(\kappa + 1)\mu}{\exp(\kappa)} \right)^{N\mu} \frac{8N\Gamma(\mu + \epsilon)w^{N\mu + \epsilon - 1 + \zeta}}{7\Gamma(\epsilon)\Gamma(N\mu + \epsilon + \zeta)\hat{w}^{N\mu + \epsilon}} \times K^\epsilon {}_2F_2\left(1, \mu + \epsilon; \epsilon, N\mu + \epsilon + \zeta; \frac{Kw}{\hat{w}}\right). \quad (37)$$

#### D. Computational Complexity and Implementation

As indicated in (12) and (22), we rely on recursion to numerically evaluate the derived expressions. A naive implementation of the proposed framework would compute the same elements multiple times, greatly increasing the computational complexity when employing a large number of terms. For instance, by using the recursion tree method, the number of computations of the type of (12) (resp. (22)) for the Extended  $\eta$ - $\mu$  (resp.  $\kappa$ - $\mu$ ) distribution amounts to  $2^\epsilon - 1$ . To reduce the computational complexity, we resort to memoization, which is a code optimization method that caches the value of every new recursive element, preventing the framework from computing it multiple times. With memoization, the number of computations of the type of (12) or (22) reduces to  $\epsilon(\epsilon + 1) - 1$ , enabling fast evaluation even with a large number of terms. Figs. 1 and 2 plot the analytical and simulated PDFs for the Extended  $\eta$ - $\mu$  and  $\kappa$ - $\mu$  distributions, respectively, with  $N = 16$  for the former and  $N = 64$  for the latter,  $\hat{w} = 1$ , and different combinations of fading parameters. The analytical PDFs are computed via (13) and (23) with truncation at  $\epsilon = 250$  terms, and strikingly agree with the simulations. Remarkably, the computation time for each curve in the plots peaks approximately at 0.5 s and the maximum absolute error with respect to the exact solutions in [21], [29] is in the order of  $10^{-16}$ .

### III. PERFORMANCE METRICS

In this section, considering the system model and the results for the Extended  $\eta$ - $\mu$  and  $\kappa$ - $\mu$  distributions derived in Section II, we obtain new expressions for the outage and coverage probability, BEP for coherent binary modulations, and SEP for  $M$ -PSK and  $M$ -QAM. To evaluate the system's

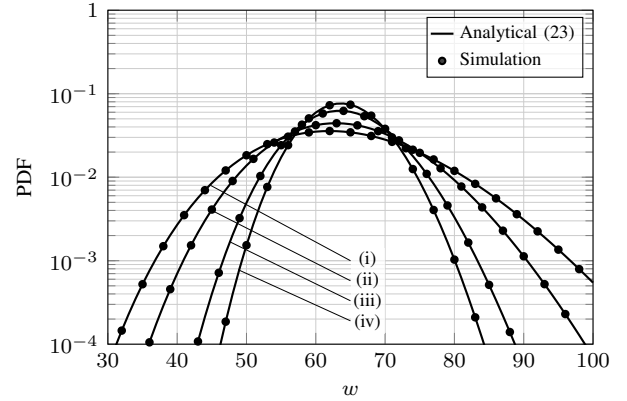


Fig. 2. PDF of the sum of squared i.i.d.  $\kappa$ - $\mu$  RVs, with  $N = 64$ ,  $\hat{w} = 1$ , and the following combinations of parameters: (i)  $\kappa \rightarrow 0$ ,  $\mu = 0.5$  (Nakagami- $m$ ); (ii)  $\kappa = 1.5$ ,  $\mu = 0.5$ ; (iii)  $\kappa = 1.5$ ,  $\mu = 1$  (Rice); and (iv)  $\kappa = 1.5$ ,  $\mu = 1.5$ .

performance at high SNR, we further derive the asymptotic expressions for these metrics.

#### A. Outage and Coverage Probabilities

The outage probability is defined as the probability that the instantaneous SNR drops below a given threshold. In this setting, the outage probability is formulated in terms of the CDF of the instantaneous SNR, i.e.,  $P_{\text{out}} = F_\gamma(\gamma_{\text{th}})$ , where  $\gamma_{\text{th}}$  is the SNR threshold. Hence, the outage probability for the Extended  $\eta$ - $\mu$  and  $\kappa$ - $\mu$  models is readily available from (14) and (24), where  $\hat{w}$  is the scale parameter that can be used to model the path loss. The coverage probability is complementary to the outage probability and is thus formulated in terms of the complementary CDF of the instantaneous SNR, i.e.,  $P_{\text{cov}} = 1 - P_{\text{out}} = 1 - F_\gamma(\gamma_{\text{th}})$ .

To derive the asymptotic expressions for the outage probability at high SNR, as done in [28], we use only the first term of the summation (corresponding to  $m = 0$ ) in (14) and (24), resulting in

$$P_{\text{out}} \sim \frac{1}{\Gamma(N\mu + 1)} \left( \left( \frac{p}{\eta} \right)^{\frac{p}{1+p}} \frac{\xi \gamma_{\text{th}}}{\hat{w}} \right)^{N\mu} \quad (38)$$

for the Extended  $\eta$ - $\mu$  model<sup>1</sup> and in

$$P_{\text{out}} \sim \frac{1}{\Gamma(N\mu + 1)} \left( \frac{(\kappa + 1)\mu\gamma_{\text{th}}}{\exp(\kappa)\hat{w}} \right)^{N\mu} \quad (39)$$

for the  $\kappa$ - $\mu$  model.

#### B. BEP for Coherent Binary Modulations

In this section, we focus on the (uncoded) BEP for coherent binary modulations. First, we obtain new expressions for the BEP by resorting to the PDFs in (13) and (23) for the Extended  $\eta$ - $\mu$  and  $\kappa$ - $\mu$  models, respectively, along with their asymptotic expressions at high SNR. Then, by deriving an upper bound on the BEP, we determine the convergence conditions for these expressions, which prove to be quite restrictive. To guarantee the convergence for any choice of parameters, we thus propose alternative expressions for the BEP based on the PDFs in (18)

<sup>1</sup>Note that (38) can also be obtained as a special case of the expression provided in [21] for the sum of squared independent but not identically distributed Extended  $\eta$ - $\mu$  RVs.

and (27) for the Extended  $\eta$ - $\mu$  and  $\kappa$ - $\mu$  models, respectively. Lastly, we obtain an upper bound on the truncation error.

The BEP for coherent binary modulations is defined as [35, Eq. (9.3)]

$$\text{BEP} = \frac{1}{2} \int_0^\infty \text{erfc}(\sqrt{g_b w}) f_W(w) dw, \quad (40)$$

with  $g_b = 1$  for coherent binary phase-shift keying (BPSK),  $g_b = 1/2$  for coherent orthogonal binary frequency-shift keying (BFSK), and  $g_b = 0.715$  for coherent BFSK with minimal correlation [35]. In our case,  $f_W(w)$  is replaced by the PDFs in (13) and (23) (or (18) and (27)).

**Approach 1.** By substituting (13) and (23) into (40), we obtain the BEP as

$$\text{BEP}_\eta = \frac{1}{2\sqrt{\pi}} \left( \frac{\left(\frac{p}{\eta}\right)^{\frac{\mu p}{1+p}} \xi^\mu}{\Gamma\left(\frac{\mu p}{1+p}\right)} \right)^N \sum_{m=0}^{\infty} \left( \frac{1}{g_b \hat{w}} \right)^{N\mu+m} \times \frac{\Gamma(N\mu+m+\frac{1}{2}) h_m}{\Gamma(N\mu+m+1)} \quad (41)$$

for the Extended  $\eta$ - $\mu$  model and as

$$\text{BEP}_\kappa = \frac{1}{2\sqrt{\pi}} \left( \frac{(\kappa+1)\mu}{\exp(\kappa)} \right)^{N\mu} \sum_{m=0}^{\infty} \left( \frac{1}{g_b \hat{w}} \right)^{N\mu+m} \times \frac{\Gamma(N\mu+m+\frac{1}{2}) k_m}{\Gamma(N\mu+m+1)} \quad (42)$$

for the  $\kappa$ - $\mu$  model.

To derive the asymptotic expressions for the BEP at high SNR, we use only the first term of the summation (corresponding to  $m=0$ ) in (41) and (42), resulting in

$$\text{BEP}_\eta \sim \frac{\Gamma(N\mu+\frac{1}{2})}{2\sqrt{\pi}\Gamma(N\mu+1)} \left( \left( \frac{p}{\eta} \right)^{\frac{p}{1+p}} \frac{\xi}{g_b \hat{w}} \right)^{N\mu} \quad (43)$$

for the Extended  $\eta$ - $\mu$  model and

$$\text{BEP}_\kappa \sim \frac{\Gamma(N\mu+\frac{1}{2})}{2\sqrt{\pi}\Gamma(N\mu+1)} \left( \frac{(\kappa+1)\mu}{\exp(\kappa)g_b \hat{w}} \right)^{N\mu} \quad (44)$$

for the  $\kappa$ - $\mu$  model.

Now, following similar steps as in Section II-C, we upper bound (41) and (42) as

$$\mathcal{C}_\eta < \frac{|h_0|}{\hat{w}^{N\mu}} \left( \frac{\Gamma(N\mu+\frac{1}{2})}{\Gamma(N\mu+1)} + \frac{8N\Gamma(\mu+1)\Gamma(N\mu+\frac{3}{2})}{7\Gamma(N\mu+2)} \right) \times \frac{w\xi p}{\hat{w}\eta} {}_2F_1\left(\mu+1; N\mu+\frac{3}{2}; N\mu+2; \frac{w\xi p}{\hat{w}\eta}\right), \quad (45)$$

and

$$\mathcal{C}_\kappa < \frac{1}{\hat{w}^{N\mu}} \left( \frac{\Gamma(N\mu+\frac{1}{2})}{\Gamma(N\mu+1)} + \frac{8N\Gamma(\mu+1)\Gamma(N\mu+\frac{3}{2})}{7\Gamma(N\mu+2)} \right) \times \frac{K}{g_b \hat{w}} {}_2F_1\left(\mu+1; N\mu+\frac{3}{2}; N\mu+2; \frac{K}{g_b \hat{w}}\right), \quad (46)$$

respectively. Despite the strict convergence interval of the Gauss hypergeometric function  ${}_2F_1$ , common mathematical packages such as Mathematica and SciPy provide solutions to arguments outside the convergence interval through its analytical continuation. In our case, this feature could not be straightforwardly exploited for the summations in (41) and (42), restricting their convergence to choice of parameters

satisfying  $|\xi p/(\eta g_b \hat{w})| < 1$  and  $|K/(g_b \hat{w})| < 1$ , respectively. To circumvent this issue and guarantee the convergence for any choice of parameters, we propose alternative expressions in the following.

**Approach 2.** By substituting (18) and (27) into (40), we obtain alternative BEP expression as

$$\text{BEP}_\eta = \left( \frac{\left(\frac{p}{\eta}\right)^{\frac{\mu p}{1+p}}}{\Gamma\left(\frac{\mu p}{1+p}\right)} \right)^N \sum_{m=0}^{\infty} \frac{\Gamma(N\mu+m+\frac{1}{2}) \left(\frac{\xi}{g_b \hat{w}}\right)^{N\mu+m} \tilde{h}_m}{2\sqrt{\pi}\Gamma(N\mu+m+1)} \times {}_2F_1\left(N\mu+m, N\mu+m+\frac{1}{2}; N\mu+m+1; \frac{-\xi}{g_b \hat{w}}\right) \quad (47)$$

for the Extended  $\eta$ - $\mu$  distribution (cf. (41)) and as

$$\text{BEP}_\kappa = \sum_{m=0}^{\infty} \frac{\Gamma(N\mu+m+\frac{1}{2}) \left(\frac{\tilde{K}}{g_b \hat{w}}\right)^{N\mu+m} \tilde{k}_m}{2\sqrt{\pi} \exp(N\kappa\mu)\Gamma(N\mu+m+1)} {}_2F_1\left(N\mu+m, N\mu+m+\frac{1}{2}; N\mu+m+1; \frac{-\tilde{K}}{g_b \hat{w}}\right) \quad (48)$$

for the  $\kappa$ - $\mu$  distribution as (cf. (42)). As commented above, (47) and (48) allow to evaluate the BEP for any choice of parameters at the cost of a slight increase in mathematical and computational complexity due to the presence of the Gauss hypergeometric function  ${}_2F_1$ . However, the latter can be drastically reduced by using its recurrence property [36, Eq. (15.5.E19)].

**Upper Bound on the Truncation Error.** An upper bound on the truncation error for the BEP is obtained by replicating the steps in Section II-C. The following expressions are suitable for both the approaches described above. Hence, an upper bound on the truncation error for the BEP is given by

$$\mathcal{E}_\eta(\epsilon) < {}_3F_2\left(N\mu+\epsilon+\frac{1}{2}, \mu+\epsilon, 1; N\mu+\epsilon+1, \epsilon; \frac{\xi p}{g_b \hat{w}\eta}\right) \times \frac{4N\Gamma(\mu+\epsilon)\Gamma(N\mu+\epsilon+\frac{1}{2})}{7\sqrt{\pi}\Gamma(\epsilon)\Gamma(N\mu+\epsilon+1)} \left( \frac{\xi p}{\eta g_b \hat{w}} \right)^\epsilon \times \left( \frac{\left(\frac{p}{\eta}\right)^{\frac{\mu p}{1+p}}}{\Gamma\left(\frac{\mu p}{1+p}\right)(g_b \hat{w})^\mu} \right)^{N\mu} \quad (49)$$

for the Extended  $\eta$ - $\mu$  model and

$$\mathcal{E}_\kappa(\epsilon) < {}_3F_2\left(N\mu+\epsilon+\frac{1}{2}, \mu+\epsilon, 1; N\mu+\epsilon+1, \epsilon; \frac{K}{g_b \hat{w}}\right) \times \frac{4N\Gamma(\mu+\epsilon)\Gamma(N\mu+\epsilon+\frac{1}{2})}{7\sqrt{\pi}\Gamma(\epsilon)\Gamma(N\mu+\epsilon+1)} \left( \frac{K}{g_b \hat{w}} \right)^\epsilon \times \left( \frac{(\kappa+1)\mu}{\exp(\kappa)g_b \hat{w}} \right)^{N\mu} \quad (50)$$

for the  $\kappa$ - $\mu$  model.

### C. SEP for M-PSK and M-QAM

In this section, we focus on the (uncoded) SEP for  $M$ -PSK and  $M$ -QAM. Specifically, we obtain new expressions for the SEP by resorting to the MGFs in (11) and (16) for the Extended  $\eta$ - $\mu$  model, and in (21) and (25) for the  $\kappa$ - $\mu$  model. As for the BEP in the previous section, the first expression for each model has lower computational complexity but quite restrictive convergence conditions (approach 1), whereas the second has slightly higher computational complexity and no restrictions on

$$\text{SEP}_\eta^{M\text{-PSK}} = \left( \frac{\left(\frac{p}{\eta}\right)^{\frac{\mu p}{1+p}}}{\Gamma\left(\frac{\mu p}{1+p}\right)} \right)^N \sum_{m=0}^{\infty} \tilde{h}_m \left( \frac{\cos\left(\frac{\pi}{M}\right)}{\pi} \left( \frac{1}{1 + \frac{g_p \hat{w}}{\xi}} \right)^{N\mu+m} F_1 \left( \frac{1}{2}; \frac{1}{2} - N\mu - m, N\mu + m; \frac{3}{2}; \cos^2 \left( \frac{\pi}{M} \right), \frac{\cos^2 \left( \frac{\pi}{M} \right)}{1 + \frac{g_p \hat{w}}{\xi}} \right) \right. \\ \left. + \left( \frac{\xi}{g_p \hat{w}} \right)^{N\mu+m} \frac{\Gamma(N\mu + m + \frac{1}{2})}{2\sqrt{\pi}\Gamma(N\mu + m + 1)} {}_2F_1 \left( N\mu + m, N\mu + m + \frac{1}{2}; N\mu + m + 1; -\frac{\xi}{g_p \hat{w}} \right) \right) \quad (53)$$

$$\text{SEP}_\kappa^{M\text{-PSK}} = \exp(-N\kappa\mu) \sum_{m=0}^{\infty} \tilde{k}_m \left( \frac{\cos\left(\frac{\pi}{M}\right)}{\pi} \left( \frac{1}{1 + \frac{g_p \hat{w}}{K}} \right)^{N\mu+m} F_1 \left( \frac{1}{2}; \frac{1}{2} - N\mu - m, N\mu + m; \frac{3}{2}; \cos^2 \left( \frac{\pi}{M} \right), \frac{\cos^2 \left( \frac{\pi}{M} \right)}{1 + \frac{g_p \hat{w}}{K}} \right) \right. \\ \left. + \left( \frac{\tilde{K}}{g_p \hat{w}} \right)^{N\mu+m} \frac{\Gamma(N\mu + m + \frac{1}{2})}{2\sqrt{\pi}\Gamma(N\mu + m + 1)} {}_2F_1 \left( N\mu + m, N\mu + m + \frac{1}{2}; N\mu + m + 1; -\frac{\tilde{K}}{g_p \hat{w}} \right) \right) \quad (55)$$

the convergence (approach 2). From the first set of expressions, we also derive the asymptotic SEP at high SNR.

**M-PSK Modulation.** The SEP for M-PSK is defined as [35, Eq. (9.15)]

$$\text{SEP}^{M\text{-PSK}} = \frac{1}{\pi} \int_0^{\frac{(M-1)\pi}{M}} \mathcal{M}_W \left( \frac{g_p}{\sin^2 \phi} \right) d\phi, \quad (51)$$

with  $g_p = \sin^2(\pi/M)$ .

For the Extended  $\eta$ - $\mu$  model, the SEP can be expressed as

$$\text{SEP}_\eta^{M\text{-PSK}} = \left( \frac{\left(\frac{p}{\eta}\right)^{\frac{\mu p}{1+p}} \xi^\mu}{\Gamma\left(\frac{\mu p}{1+p}\right)} \right)^N \sum_{m=0}^{\infty} \left( \frac{1}{g_p \hat{w}} \right)^{N\mu+m} \frac{h_m}{2\pi} \\ \times \left( \frac{2\sqrt{\pi}\Gamma(N\mu + m + \frac{1}{2})}{\Gamma(N\mu + m + 1)} \right. \\ \left. - B \left( \sin^2 \left( \frac{\pi}{M} \right); N\mu + m + \frac{1}{2}, \frac{1}{2} \right) \right) \quad (52)$$

for the MGF in (11) and as in (53) at the top of the page for the MGF in (16).

For the  $\kappa$ - $\mu$  model, the SEP can be expressed as

$$\text{SEP}_\kappa^{M\text{-PSK}} = \left( \frac{(\kappa + 1)\mu}{\exp(\kappa)} \right)^{N\mu} \sum_{m=0}^{\infty} \left( \frac{1}{g_p \hat{w}} \right)^{N\mu+m} \frac{k_m}{2\pi} \\ \times \left( \frac{2\sqrt{\pi}\Gamma(N\mu + m + \frac{1}{2})}{\Gamma(N\mu + m + 1)} \right. \\ \left. - B \left( \sin^2 \left( \frac{\pi}{M} \right); N\mu + m + \frac{1}{2}, \frac{1}{2} \right) \right) \quad (54)$$

for the MGF in (21) and as in (55) at the top of the page for the MGF in (25).

To derive the asymptotic expressions for the SEP at high SNR, we use only the first term of the summation (corresponding to  $m = 0$ ) in (52) and (54), resulting in

$$\text{SEP}_\eta^{M\text{-PSK}} \sim \frac{1}{2\pi} \left( \left( \frac{p}{\eta} \right)^{\frac{\mu p}{1+p}} \frac{\xi}{g_p \hat{w}} \right)^{N\mu} \left( \frac{2\sqrt{\pi}\Gamma(N\mu + \frac{1}{2})}{\Gamma(N\mu + 1)} \right. \\ \left. - B \left( \sin^2 \left( \frac{\pi}{M} \right); N\mu + \frac{1}{2}, \frac{1}{2} \right) \right) \quad (56)$$

for the Extended  $\eta$ - $\mu$  model and

$$\text{SEP}_\kappa^{M\text{-PSK}} \sim \frac{1}{2\pi} \left( \frac{(\kappa + 1)\mu}{\exp(\kappa)g_p \hat{w}} \right)^{N\mu} \left( \frac{2\sqrt{\pi}\Gamma(N\mu + \frac{1}{2})}{\Gamma(N\mu + 1)} \right. \\ \left. - B \left( \sin^2 \left( \frac{\pi}{M} \right); N\mu + \frac{1}{2}, \frac{1}{2} \right) \right) \quad (57)$$

for the  $\kappa$ - $\mu$  model.

**M-QAM Modulation.** The SEP for M-QAM is defined as [35, Eq. (9.21)]

$$\text{SEP}^{M\text{-QAM}} = \frac{4}{\pi} \left( 1 - \frac{1}{\sqrt{M}} \right) \int_0^{\pi/2} \mathcal{M}_W \left( \frac{g_q}{\sin^2 \phi} \right) d\phi \\ - \frac{4}{\pi} \left( 1 - \frac{1}{\sqrt{M}} \right)^2 \int_0^{\pi/4} \mathcal{M}_W \left( \frac{g_q}{\sin^2 \phi} \right) d\phi, \quad (58)$$

with  $g_q = 3/(2(M-1))$ .

For the Extended  $\eta$ - $\mu$  model, the SEP can be expressed as

$$\text{SEP}_\eta^{M\text{-QAM}} = \frac{2}{\sqrt{\pi}} \left( \frac{\left(\frac{p}{\eta}\right)^{\frac{\mu p}{1+p}} \xi^\mu}{\Gamma\left(\frac{\mu p}{1+p}\right)} \right)^N \sum_{m=0}^{\infty} \left( \frac{1}{g_q \hat{w}} \right)^{N\mu+m} \\ \times h_m \left( 1 - \frac{1}{\sqrt{M}} \right) \left( \frac{\Gamma(N\mu + m + \frac{1}{2})}{\Gamma(N\mu + m + 1)} \right. \\ \left. - \frac{1 - \frac{1}{\sqrt{M}}}{\sqrt{\pi}} B \left( \frac{1}{2}; N\mu + m + \frac{1}{2}, \frac{1}{2} \right) \right) \quad (59)$$

for the MGF in (11) and as in (60) at the top of the next page for the MGFs in (16).

For the  $\kappa$ - $\mu$  model, the SEP can be expressed as

$$\text{SEP}_\kappa^{M\text{-QAM}} = \frac{2}{\sqrt{\pi}} \left( \frac{(\kappa + 1)\mu}{\exp(\kappa)} \right)^{N\mu} \sum_{m=0}^{\infty} \left( \frac{1}{g_q \hat{w}} \right)^{N\mu+m} \\ \times k_m \left( 1 - \frac{1}{\sqrt{M}} \right) \left( \frac{\Gamma(N\mu + m + \frac{1}{2})}{\Gamma(N\mu + m + 1)} \right. \\ \left. - \frac{1 - \frac{1}{\sqrt{M}}}{\sqrt{\pi}} B \left( \frac{1}{2}; N\mu + m + \frac{1}{2}, \frac{1}{2} \right) \right) \quad (61)$$

for the MGF in (21) and as in (62) at the top of the next page for the MGF in (25).

To derive the asymptotic expressions for the SEP at high SNR, we use only the first term of the summation (correspond-

$$\begin{aligned} \text{SEP}_\eta^{M\text{-QAM}} &= \left( \frac{\left(\frac{p}{\eta}\right)^{\frac{\mu p}{1+p}}}{\Gamma\left(\frac{\mu p}{1+p}\right)} \right)^N \sum_{m=0}^{\infty} \frac{2(\sqrt{M}-1)\tilde{h}_m}{M\pi} \left( \frac{\sqrt{\pi}\Gamma(N\mu+m+\frac{1}{2})}{\Gamma(N\mu+m)} \left( \frac{\sqrt{M}}{(-1)^{N\mu+m}} B_{\frac{-\xi}{g_q\hat{w}}} \left( N\mu+m, \frac{1}{2} - N\mu - m \right) \right. \right. \\ &\quad \left. \left. - (\sqrt{M}-1)B\left(\frac{\xi}{g_q\hat{w}+\xi}; N\mu+m, \frac{1}{2}\right) \right) + \sqrt{2}(\sqrt{M}-1) \left( \frac{\xi}{g_q\hat{w}+\xi} \right)^{N\mu+m} \right. \\ &\quad \left. \times F_1\left(\frac{1}{2}; \frac{1}{2} - N\mu - m, N\mu+m; \frac{3}{2}; \frac{1}{2}, \frac{\xi}{2(g_q\hat{w}+\xi)}\right) \right) \end{aligned} \quad (60)$$

$$\begin{aligned} \text{SEP}_\kappa^{M\text{-QAM}} &= \sum_{m=0}^{\infty} \frac{2(\sqrt{M}-1)\tilde{k}_m}{M\pi \exp(N\kappa\mu)} \left( \frac{\sqrt{\pi}\Gamma(N\mu+m+\frac{1}{2})}{\Gamma(N\mu+m)} \left( \frac{\sqrt{M}}{(-1)^{N\mu+m}} B\left(\frac{-\tilde{K}}{g_q\hat{w}}; N\mu+m, \frac{1}{2} - N\mu - m \right) \right. \right. \\ &\quad \left. \left. - (\sqrt{M}-1)B\left(\frac{\tilde{K}}{\tilde{K}+g_q\hat{w}}; N\mu+m, \frac{1}{2}\right) \right) + \sqrt{2}(\sqrt{M}-1) \left( \frac{\tilde{K}}{\tilde{K}+g_q\hat{w}} \right)^{N\mu+m} \right. \\ &\quad \left. \times F_1\left(\frac{1}{2}; \frac{1}{2} - N\mu - m, N\mu+m; \frac{3}{2}; \frac{1}{2}, \frac{\tilde{K}}{2(\tilde{K}+g_q\hat{w})}\right) \right) \end{aligned} \quad (62)$$

	Extended $\eta$ - $\mu$		$\kappa$ - $\mu$	
MGF	(11)	(16)	(21)	(25)
PDF	(13)	(18)	(23)	(27)
CDF (outage probability)	(14)	(19)	(24)	(28)
↳ high SNR	(38)		(39)	
BEP	(41)	(47)	(42)	(48)
↳ high SNR	(43)		(44)	
SEP for $M$ -PSK	(52)	(53)	(54)	(55)
↳ high SNR	(56)		(57)	
SEP for $M$ -QAM	(59)	(60)	(61)	(62)
↳ high SNR	(63)		(64)	

Table I. Summary of derived expressions. For each model, the expressions in the first column have lower computational complexity but quite restrictive convergence conditions, whereas those in the second column have slightly higher computational complexity and no restrictions on the convergence.

ing to  $m = 0$ ) in (59) and (61), resulting in

$$\begin{aligned} \text{SEP}_\eta^{M\text{-QAM}} &\sim \frac{2\left(1 - \frac{1}{\sqrt{M}}\right)}{\sqrt{\pi}} \left( \left(\frac{p}{\eta}\right)^{\frac{p}{1+p}} \frac{\xi}{g_q\hat{w}} \right)^{N\mu} \left( \frac{\Gamma(N\mu + \frac{1}{2})}{\Gamma(N\mu + 1)} \right. \\ &\quad \left. - \frac{1 - \frac{1}{\sqrt{M}}}{\sqrt{\pi}} B\left(\frac{1}{2}; N\mu + \frac{1}{2}, \frac{1}{2}\right) \right) \end{aligned} \quad (63)$$

for the Extended  $\eta$ - $\mu$  model and

$$\begin{aligned} \text{SEP}_\kappa^{M\text{-QAM}} &\sim \frac{2\left(1 - \frac{1}{\sqrt{M}}\right)}{\sqrt{\pi}} \left( \frac{(\kappa + 1)\mu}{\exp(\kappa)g_q\hat{w}} \right)^{N\mu} \left( \frac{\Gamma(N\mu + \frac{1}{2})}{\Gamma(N\mu + 1)} \right. \\ &\quad \left. - \frac{1 - \frac{1}{\sqrt{M}}}{\sqrt{\pi}} B\left(\frac{1}{2}; N\mu + \frac{1}{2}, \frac{1}{2}\right) \right) \end{aligned} \quad (64)$$

for the  $\kappa$ - $\mu$  model.

#### IV. PERFORMANCE EVALUATION

In this section, we build on the proposed framework for the Extended  $\eta$ - $\mu$  and  $\kappa$ - $\mu$  models to analyze the performance of a downlink system operating in FR3 and the sub-THz band, respectively. As in the system model described in Section II, we consider a single-antenna user served by a multi-antenna BS employing MRT, with perfect and imperfect CSI at the latter.

We compare the analytical results (obtained using Mathematica on a standard off-the-shelf laptop computer) with Monte Carlo simulations. In all the plots, the lines indicate the analytical results obtained with the proposed framework (summarized in Table I) and the markers represent the simulation results, which are in agreement with the analytical results.

We assume a log-distance path loss model according to which we have  $\hat{w} = \frac{P_t}{\sigma^2} \varphi d^{-\beta}$ , where  $\varphi$  represents the frequency-dependent path loss factor referenced at 1 m,  $d$  denotes the distance between the BS and the user, and  $\beta$  indicates the path loss exponent. The path loss factor is defined as  $\varphi = (c/(4\pi f_c))^2$ , where  $c$  represents the speed of light and  $f_c$  denotes the carrier frequency. The noise power is calculated as  $\sigma^2 = -174 + 10 \log_{10} \Omega + \nu$  (measured in dBm), where  $\Omega$  denotes the transmission bandwidth and  $\nu = 5$  dB is the noise figure of the user. Unless otherwise stated, we fix  $P_t = 30$  dBm and assume perfect CSI at the BS (i.e.,  $\alpha = 0$ ).

##### A. FR3 System Modeled with Extended $\eta$ - $\mu$ Fading

In this section, we evaluate the performance of an FR3 system with dominant NLoS components using the Extended  $\eta$ - $\mu$  model. The NLoS-dominated propagation is imposed through the path loss exponent  $\beta = 3$ . We assume that the bandwidth is 3% of the carrier frequency, i.e.,  $\Omega = 0.03f_c$ , as in [4]. Unless otherwise stated, we assume  $f_c = 15$  GHz,  $d = 250$  m, and severe fading conditions characterized by  $\eta = 1.5$ ,  $\mu = 0.5$ , and  $p = 0.75$ . For the number of antennas, we set  $N \in \{16, 32, 64, 128, 256\}$ .

Fig. 3 depicts the coverage probability versus the distance between the BS and the user, with SNR threshold  $\gamma_{\text{th}} \in \{0, 5\}$  dB. As expected, the coverage improves significantly as the number of antennas increases. For instance, using  $N = 256$  allows to achieve perfect coverage up to approximately 300 m and 450 m with  $\gamma_{\text{th}} = 5$  dB and  $\gamma_{\text{th}} = 0$  dB, respectively. The analytical results are computed with 100 terms and the entire plot takes about 1 s to generate. For comparison, the expression in [21] takes up to 100 s per point with  $N = 16$  and, as the number of antenna increases, the computation time grows significantly

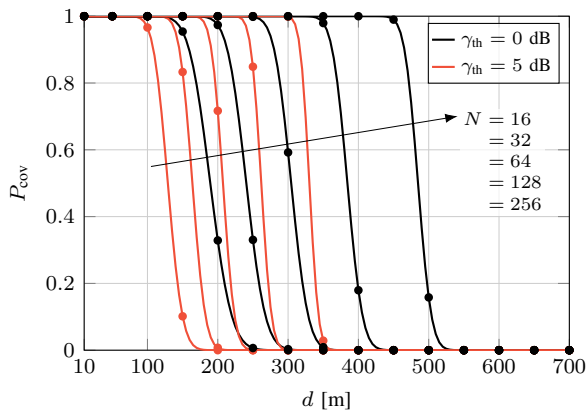


Fig. 3. Extended  $\eta$ - $\mu$  model: Downlink coverage probability versus distance, with  $\eta = 1.5$ ,  $\mu = 0.5$ ,  $p = 0.75$ ,  $f_c = 15$  GHz,  $P_t = 30$  dBm,  $N \in \{16, 32, 64, 128, 256\}$ ,  $\alpha = 0$ , and  $\gamma_{th} \in \{0, 5\}$  dB.

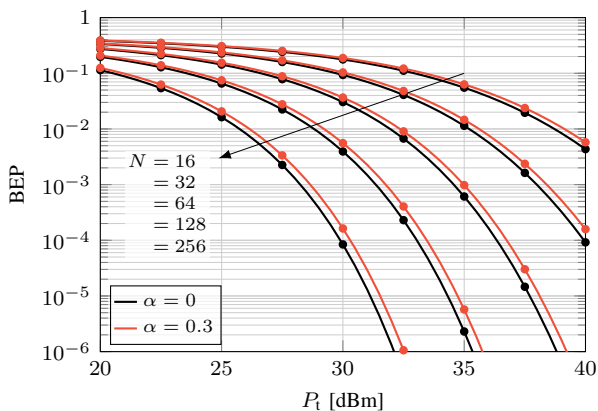


Fig. 4. Extended  $\eta$ - $\mu$  model: Downlink BEP for coherent BPSK versus transmit power, with  $\eta = 1.5$ ,  $\mu = 0.5$ ,  $p = 0.75$ ,  $f_c = 15$  GHz,  $d = 250$  m,  $N \in \{16, 32, 64, 128, 256\}$ , and  $\alpha \in \{0, 0.3\}$ .

and eventually the expression fails to converge to the correct value.

Fig. 4 shows the BEP for coherent BPSK versus the transmit power. We assume perfect and imperfect CSI with  $\alpha \in \{0, 0.3\}$ . Again, we emphasize the benefits of increasing the number of antennas. For  $P_t = 30$  dBm and  $\alpha = 0$ , doubling the number of antennas from  $N = 128$  to  $N = 256$  yields a  $50\times$  reduction in the BEP, i.e., from  $4 \times 10^{-3}$  to  $8 \times 10^{-5}$ . The analytical results are computed with 200 terms, remarkably taking less than 2 s to generate the whole plot.

Fig. 5 plots the BEP for coherent BPSK versus the carrier frequency, again with  $\alpha \in \{0, 0.3\}$ . In this setting, the carrier frequency can be increased as the number of antennas grows. For example, fixing a target BEP of  $10^{-3}$ , increasing the number of antennas from  $N = 32$  to  $N = 256$  allows to extend the carrier frequency approximately from 8 GHz to 17 GHz and the corresponding bandwidth from about 240 MHz to 510 MHz.

Fig. 6 illustrates the BEP for coherent BPSK versus the carrier frequency, with  $N = 64$ . We consider five combinations of fading parameters modeling fading conditions ranging from very severe to favorable: (i)  $\eta = 1.5$ ,  $\mu = 0.25$ ,  $p = 0.25$  (black line); (ii)  $\eta = 1.5$ ,  $\mu = 0.5$ ,  $p = 0.25$  (red line); (iii)  $\eta = 1.5$ ,  $\mu = 0.5$ ,  $p = 0.75$  (black dashed line); (iv)  $\eta = 0.8$ ,

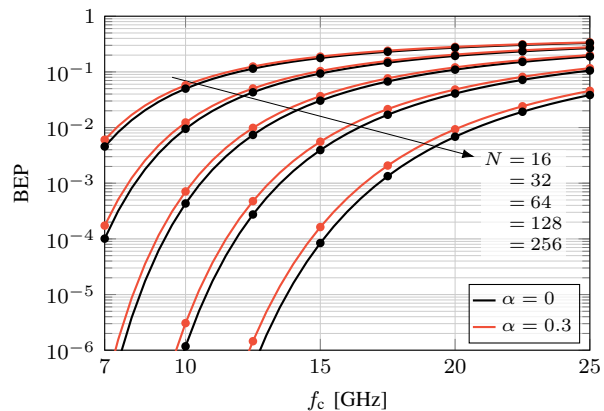


Fig. 5. Extended  $\eta$ - $\mu$  model: Downlink BEP for coherent BPSK versus carrier frequency, with  $\eta = 1.5$ ,  $\mu = 0.5$ ,  $p = 0.75$ ,  $d = 250$  m,  $P_t = 30$  dBm,  $N \in \{16, 32, 64, 128, 256\}$ , and  $\alpha \in \{0, 0.3\}$ .

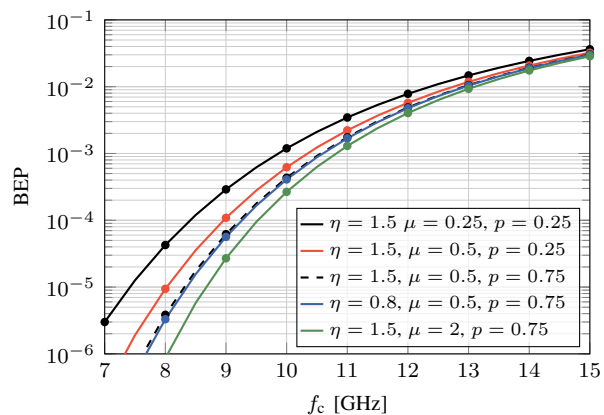


Fig. 6. Extended  $\eta$ - $\mu$  model: Downlink BEP for coherent BPSK versus carrier frequency, with  $\eta \in \{0.8, 1.5\}$ ,  $\mu \in \{0.25, 0.5, 2\}$ ,  $p \in \{0.25, 0.75\}$ ,  $d = 250$  m,  $P_t = 30$  dBm,  $N = 64$ , and  $\alpha = 0$ .

$\mu = 0.5$ ,  $p = 0.75$  (blue line); and (v)  $\eta = 1.5$ ,  $\mu = 2$ ,  $p = 0.75$  (green line). In (i), the BEP is primarily impaired due to the small values of  $\mu$  (i.e., the number of multipath clusters) and  $p$  (i.e., the ratio between the numbers of multipath clusters of the in-phase and of the quadrature components). In (ii), by doubling  $\mu$ , the BEP improves significantly since the array gain highly depends on  $\mu$ . Furthermore, increasing  $p$  in (iii) yields a smaller but noteworthy improvement. In (iv), by decreasing  $\eta$  (i.e., the power ratio between the in-phase and quadrature signals) such that  $\eta \rightarrow p$ , the BEP decreases only marginally. Lastly, in (v), by increasing  $\mu$  (again with  $\eta = 1.5$ ), we observe a further improvement in the BEP.

Fig. 7 depicts the SEP for  $M$ -PSK and  $M$ -QAM versus the transmit power, with  $N = 256$  and modulation orders  $M_{PSK} \in \{4, 8, 16\}$  and  $M_{QAM} \in \{8, 16, 32, 64\}$ . Note that 4-QAM is omitted since it coincides with 4-PSK. Evidently, the SEP worsens as the modulation order increases. Furthermore, for fixed modulation order,  $M$ -QAM yields a better performance compared with  $M$ -PSK due to the larger distance between the constellation points.

Lastly, Fig. 8 shows the asymptotic BEP for coherent BPSK along with the asymptotic SEP for 4-PSK and 8-QAM at high SNR versus the transmit power. To observe the asymptotic behavior (dotted lines), we reduce the distance and the number

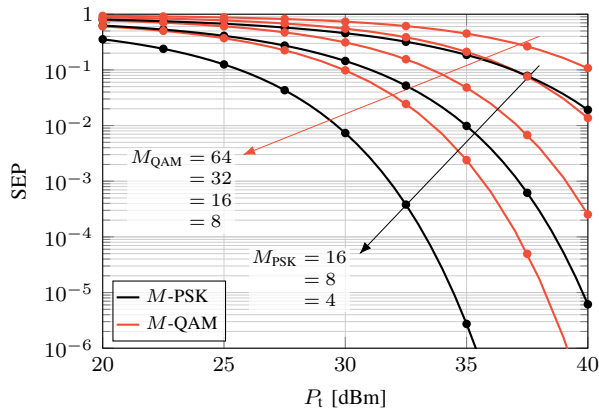


Fig. 7. Extended  $\eta$ - $\mu$  model: Downlink SEP for  $M$ -PSK and  $M$ -QAM versus transmit power, with  $\eta = 1.5$ ,  $\mu = 0.5$ ,  $p = 0.75$ ,  $f_c = 15$  GHz,  $d = 250$  m,  $P_t = 30$  dBm,  $N = 256$ ,  $\alpha = 0$ ,  $M_{\text{PSK}} \in \{4, 8, 16\}$ , and  $M_{\text{QAM}} \in \{8, 16, 32, 64\}$ .

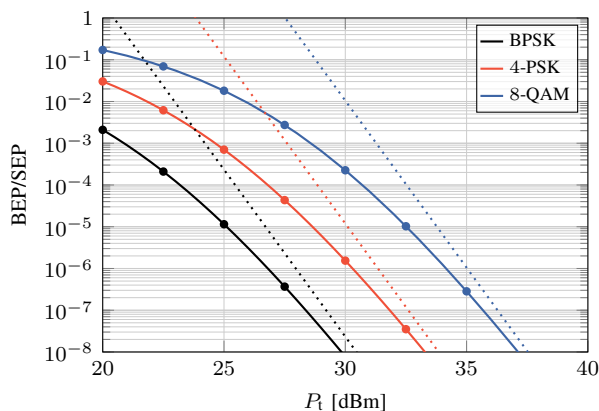


Fig. 8. Extended  $\eta$ - $\mu$  model: Downlink BEP for coherent BPSK and SEP for 4-PSK and 8-QAM versus transmit power, with  $\eta = 1.5$ ,  $\mu = 0.5$ ,  $p = 0.75$ ,  $f_c = 15$  GHz,  $d = 50$  m,  $P_t = 30$  dBm,  $N = 16$ , and  $\alpha = 0$ .

of antennas to  $d = 50$  and  $N = 16$ , respectively. In particular, the slope is mainly dictated by the number of antennas and number of multipath clusters.

### B. Sub-THz Systems Modeled with $\kappa$ - $\mu$ Fading

In this section, we evaluate the performance of a sub-THz system with dominant LoS components using the  $\kappa$ - $\mu$  model. The LoS-dominated propagation is imposed through the path loss exponent  $\beta = 2$ . We assume that the bandwidth is 1% of the carrier frequency, i.e.,  $\Omega = 0.01f_c$ , as in [37]. Unless otherwise stated, we assume  $f_c = 140$  GHz,  $d = 300$  m, and severe fading conditions characterized by  $\kappa = 0.5$  and  $\mu = 0.5$ . For the number of antennas, we set  $N \in \{64, 128, 256, 512, 1024\}$ .

Fig. 9 plots the coverage probability versus the distance between the BS and the user, with  $\gamma_{\text{th}} \in \{0, 5\}$  dB. Adopting  $N = 1024$  allows to compensate for the strong path loss at 140 GHz and achieve perfect coverage up to approximately 700 m and 1200 m for  $\gamma_{\text{th}} = 5$  dB and  $\gamma_{\text{th}} = 0$  dB, respectively. Note that this extensive coverage is primarily enabled by the truly massive number of antennas combined with the LoS-dominated propagation, in contrast with the NLoS-dominated propagation characterizing the FR3 system in Section IV-A (cf. Fig. 3). We refer to Section IV-C for further discussion. The

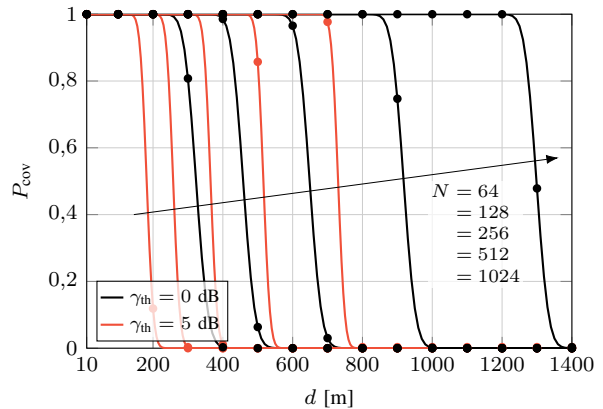


Fig. 9.  $\kappa$ - $\mu$  model: Downlink coverage probability versus distance, with  $\kappa = 0.5$ ,  $\mu = 0.5$ ,  $f_c = 140$  GHz,  $P_t = 30$  dBm,  $N \in \{64, 128, 256, 512, 1024\}$ ,  $\alpha = 0$ , and  $\gamma_{\text{th}} \in \{0, 5\}$  dB.

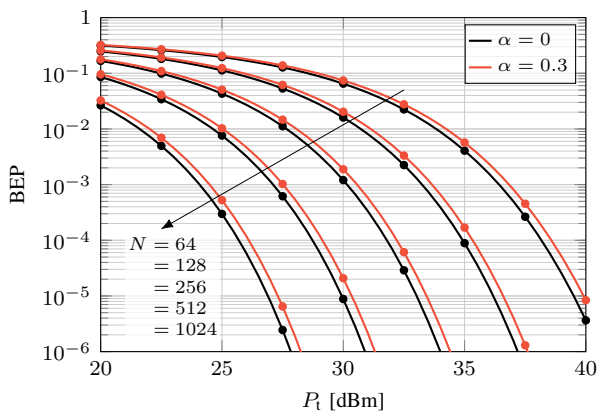


Fig. 10.  $\kappa$ - $\mu$  model: Downlink BEP for coherent BPSK versus transmit power, with  $\kappa = 0.5$ ,  $\mu = 0.5$ ,  $f_c = 140$  GHz,  $d = 300$  m,  $N \in \{64, 128, 256, 512, 1024\}$ , and  $\alpha \in \{0, 0.3\}$ .

analytical results are computed with 100 terms, remarkably taking less than 5 s to generate the whole plot. For comparison, the expression in [29] provides the same output in about 248 s.

Fig. 10 illustrates the BEP for coherent BPSK versus the transmit power, with  $\alpha \in \{0, 0.3\}$ . For  $P_t = 30$  dBm, doubling the number of antennas from  $N = 256$  to  $N = 512$  results in a  $136\times$  reduction in the BEP with  $\alpha = 0$ , i.e., from  $1.2 \times 10^{-3}$  to  $8.8 \times 10^{-6}$ . The analytical results are computed with no more than 400 terms and the entire plot takes less than 3 s to generate.

Fig. 11 depicts the BEP for coherent BPSK versus the carrier frequency, again with  $\alpha \in \{0, 0.3\}$ . Fixing a target BEP of  $10^{-3}$ , increasing the number of antennas from  $N = 128$  to  $N = 1024$  allows to expand the carrier frequency approximately from 109 GHz to 220 GHz and the corresponding bandwidth from about 1.09 GHz to 2.2 GHz.

Fig. 12 shows the BEP versus the carrier frequency, with  $N = 256$ . We consider four combinations of fading parameters mimicking fading conditions ranging from very severe to favorable: (i)  $\kappa = 0.5$ ,  $\mu = 0.25$  (black line); (ii)  $\kappa = 0.5$ ,  $\mu = 0.5$  (red line); (iii)  $\kappa = 2$ ,  $\mu = 0.5$  (blue line); and (iv)  $\kappa = 0.5$ ,  $\mu = 2$  (green line). In (i), the BEP is undermined by the small value of  $\mu$  (i.e., the number of multipath clusters). In (ii), by slightly increasing  $\mu$ , the BEP significantly improves,

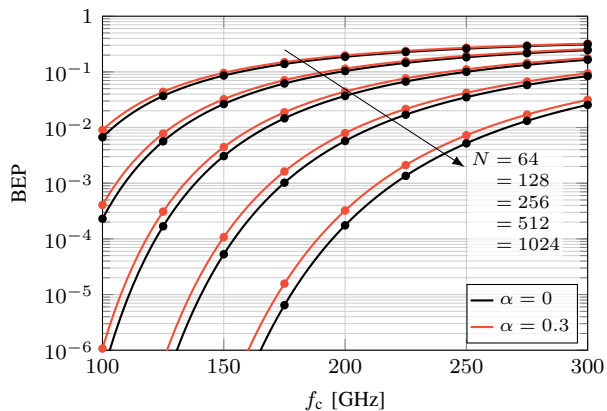


Fig. 11.  $\kappa$ - $\mu$  model: Downlink BEP for coherent BPSK versus carrier frequency, with  $\kappa = 0.5$ ,  $2\mu = 0.5$ ,  $d = 300$  m,  $P_t = 30$  dBm,  $N \in \{64, 128, 256, 512, 1024\}$ , and  $\alpha \in \{0, 0.3\}$ .

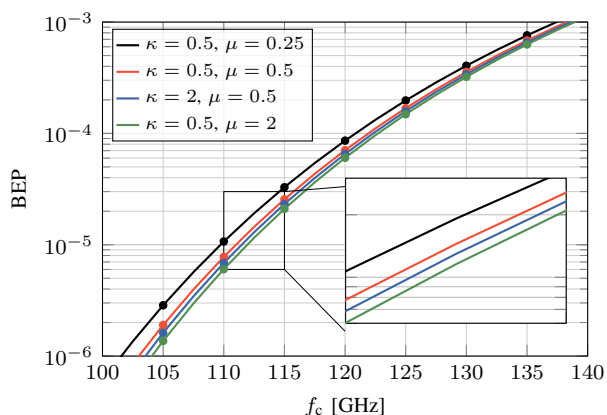


Fig. 12.  $\kappa$ - $\mu$  model: Downlink BEP for coherent BPSK versus carrier frequency, with  $\kappa \in \{0.5, 2\}$ ,  $\mu \in \{0.25, 0.5, 2\}$ ,  $d = 300$  m,  $P_t = 30$  dBm,  $N = 256$ , and  $\alpha = 0$ .

which allows to extend the carrier frequency by at least 1 GHz. In (iii), a  $4\times$  increase in  $\kappa$  (i.e., the power ratio between the LoS and NLoS components) produces only a timid decrease in the BEP since the array gain weakly depends on  $\kappa$ . Lastly, in (vi), a bigger increase in  $\mu$  yields a considerable BEP improvement, further pushing the carrier frequency up by 1 GHz. Hence, even though we consider LoS-dominated propagation, the NLoS components still have a noticeable impact on the system's performance.

Fig. 13 plots the SEP for  $M$ -PSK and  $M$ -QAM versus the transmit power, with  $N = 512$ ,  $M_{\text{PSK}} \in \{4, 8, 16\}$ , and  $M_{\text{QAM}} \in \{8, 16, 32, 64\}$ . In this setting, the SEP is lower than that of the FR3 system in Section IV-A (cf. Fig. 7): for instance, for  $P_t = 30$  dBm and 4-PSK, the SEP decreases from  $7.5 \times 10^{-3}$  to  $1.4 \times 10^{-3}$ .

Lastly, Fig. 14 illustrates the asymptotic BEP for coherent BPSK and the asymptotic SEP for 4-PSK and 8-QAM at high SNR versus the transmit power. To visualize the asymptotic behavior (dotted lines), we reduce the distance and the number of antennas to  $d = 50$  and  $N = 32$ , respectively. As in Fig. 8, the slope is mostly determined by the number of antennas and number of multipath clusters.

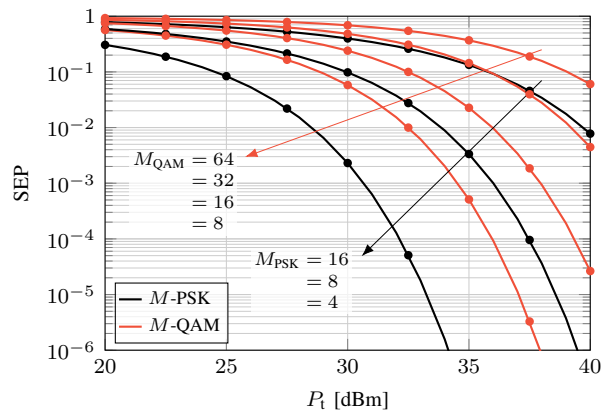


Fig. 13.  $\kappa$ - $\mu$  model: Downlink SEP for  $M$ -PSK and  $M$ -QAM versus transmit power, with  $\kappa = 0.5$ ,  $\mu = 0.5$ ,  $f_c = 140$  GHz,  $d = 300$  m,  $N = 512$ ,  $\alpha = 0$ ,  $M_{\text{PSK}} \in \{4, 8, 16\}$ , and  $M_{\text{QAM}} \in \{8, 16, 32, 64\}$ .

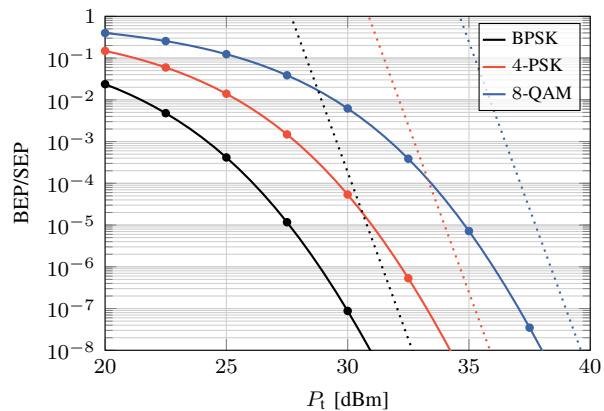


Fig. 14.  $\kappa$ - $\mu$  model: Downlink BEP for coherent BPSK and SEP for 4-PSK and 8-QAM versus transmit power, with  $\kappa = 0.5$ ,  $\mu = 0.5$ ,  $f_c = 140$  GHz,  $d = 50$  m,  $N = 32$ , and  $\alpha = 0$ .

### C. Comparison Between FR3 and Sub-THz Systems

Based on the results in Sections IV-A and IV-B, we highlight that the number of antennas  $N$ , the number of multipath clusters  $\mu$ , and the path loss exponent  $\beta$  are the key parameters that most significantly influence the system's performance. In both FR3 and sub-THz systems,  $N$  and  $\mu$  are the primary factors contributing to the array gain. We observe that an eight-fold increase in the number of antennas enables the carrier frequency (and, consequently, the bandwidth) to be approximately doubled while maintaining the same performance for both the FR3 and sub-THz systems considered. In addition, even in high-frequencies, LoS-dominated scenarios, the NLoS components continue to make a noticeable contribution to the received signal. Lastly, the LoS or NLoS path loss exponent has a greater impact on the system's performance than the frequency-dependent path loss factor. For example, compare the coverage probabilities in Fig. 3 and Fig. 9. Considering  $d = 500$  m, the path loss at  $f_c = 15$  GHz with  $\beta = 3$  is about  $5.74\times$  stronger than at  $f_c = 140$  GHz with  $\beta = 2$ . This is because the NLoS-dominated propagation considered for the FR3 system is more detrimental than the increase in carrier frequency from 15 GHz to 140 GHz. Hence, for the same number of antennas, we observe a better coverage with LoS-dominated propagation at  $f_c = 140$  GHz than with NLoS-dominated propagation at

$f_c = 15$  GHz.

## V. FINAL REMARKS

In this paper, we developed a new exact representation of the sum of squared i.i.d. Extended  $\eta$ - $\mu$  and  $\kappa$ - $\mu$  RVs. The proposed analytical framework is remarkably tractable and computationally efficient, and thus can be conveniently employed to analyze system with massive antenna arrays. We derived novel expressions for the PDF and CDF, we analyzed their convergence and truncation error, and we discussed the computational complexity and implementation aspects. Furthermore, we derived expressions for the outage and coverage probability, BEP for coherent binary modulations, and SEP for  $M$ -PSK and  $M$ -QAM. Lastly, we provided an extensive performance evaluation of FR3 and sub-THz systems focusing on a downlink scenario where a single-antenna user is served by a BS employing MRT. The results unveiled the relationship between the system's performance and parameters such as the number of antennas, the number of multipath clusters, and the path loss exponent. Future work will consider extensions to the multi-user scenario.

## REFERENCES

- [1] 3GPP, "NR; user equipment (UE) radio transmission and reception; part 1: Range 1 standalone," 2024, 38.101-1 (v18.7.0).
- [2] —, "NR; user equipment (UE) radio transmission and reception; part 2: Range 2 standalone," 2024, 38.101-2 (v18.7.0).
- [3] —, "Study on the 7 to 24 GHz frequency range for NR," 2021, 38.820 (v16.1.0).
- [4] S. Kang, M. Mezzavilla, S. Rangan, A. Madanayake, S. B. Venkatakrishnan, G. Hellboug, M. Ghosh, H. Rahmani, and A. Dhananjay, "Cellular wireless networks in the upper mid-band," *IEEE Open J. Commun. Soc.*, vol. 5, pp. 2058–2075, 2024.
- [5] N. Rajatheva, I. Atzeni, E. Björnson *et al.*, "White paper on broadband connectivity in 6G," Jun. 2020. [Online]. Available: <https://oulurepo.oulu.fi/handle/10024/36799>
- [6] C. Han, Y. Wang, Y. Li, Y. Chen, N. A. Abbasi, T. Kürner, and A. F. Molisch, "Terahertz wireless channels: A holistic survey on measurement, modeling, and analysis," *IEEE Commun. Surveys and Tuts.*, vol. 24, no. 3, pp. 1670–1707, 2022.
- [7] D. Serghiou, M. Khalily, T. W. C. Brown, and R. Tafazolli, "Terahertz channel propagation phenomena, measurement techniques and modeling for 6G wireless communication applications: A survey, open challenges and future research directions," *IEEE Commun. Surveys and Tuts.*, vol. 24, no. 4, pp. 1957–1996, 2022.
- [8] J. Ye, S. Dang, G. Ma, O. Amin, B. Shihada, and M.-S. Alouini, "On outage performance of terahertz wireless communication systems," *IEEE Trans. Commun.*, vol. 70, no. 1, pp. 649–663, 2022.
- [9] N. Iqbal, J. Luo, R. Müller, G. Steinböck, C. Schneider, D. A. Dupleich, S. Häfner, and R. S. Thomä, "Multipath cluster fading statistics and modeling in millimeter-wave radio channels," *IEEE Trans. Antennas and Propag.*, vol. 67, no. 4, pp. 2622–2632, 2019.
- [10] A. R. Ekti, A. Boyaci, A. Alparslan, İ. Ünal, S. Yarkan, A. Görçin, H. Arslan, and M. Uysal, "Statistical modeling of propagation channels for terahertz band," in *Proc. IEEE Conf. Stand. Commun. Netw. (CSCN)*, 2017.
- [11] X. Liu, L. Yang, T. Liao, Z. Luo, D. Yu, and G. Yue, "Measurements and analysis of millimeter-wave propagation from in-station to out-station in high-speed railway between train and trackside," *IEEE Trans. Wireless Commun.*, vol. 23, no. 6, pp. 5922–5937, 2024.
- [12] T. R. R. Marins, A. A. D. Anjos, C. R. N. D. Silva, V. M. R. Peñarrocha, L. Rubio, J. Reig, R. A. A. De Souza, and M. D. Yacoub, "Fading evaluation in standardized 5G millimeter-wave band," *IEEE Access*, vol. 9, pp. 67 268–67 280, 2021.
- [13] E. N. Pappasotiropoulos, A.-A. A. Boulogeorgos, K. Haneda, M. F. de Guzman, and A. Alexiou, "An experimentally validated fading model for THz wireless systems," *Sci. Rep.*, vol. 11, no. 1, p. 18717, 2021.
- [14] H. Du, J. Zhang, K. Guan, D. Niyato, H. Jiao, Z. Wang, and T. Kürner, "Performance and optimization of reconfigurable intelligent surface aided THz communications," *IEEE Trans. Commun.*, vol. 70, no. 5, pp. 3575–3593, 2022.
- [15] J. D. V. Sánchez, F. J. Lopez-Martinez, J. F. Paris, and J. M. Romero-Jerez, "The multi-cluster fluctuating two-ray fading model," *IEEE Trans. Wireless Commun.*, vol. 23, no. 5, pp. 4199–4213, 2024.
- [16] A. A. Joshi, P. Bhardwaj, and S. M. Zafaruddin, "Terahertz wireless transmissions with maximal ratio combining over fluctuating two-ray fading," in *Proc. IEEE Wireless Commun. and Netw. Conf. (WCNC)*, 2022.
- [17] N. P. Le and M.-S. Alouini, "Performance analysis of RIS-aided THz wireless systems over  $\alpha$ - $\mu$  fading: An approximate closed-form approach," *IEEE Internet of Things J.*, vol. 11, no. 1, pp. 1328–1343, 2024.
- [18] R. Premanand, N. Vishwakarma, R. Singh, and A. S. Madhukumar, "Intelligent reflecting surfaces-assisted hybrid THz/RF system over generalized fading," in *Proc. IEEE Int. Conf. Commun. (ICC)*, 2024.
- [19] S. Li and L. Yang, "Performance analysis of dual-hop THz transmission systems over  $\alpha$ - $\mu$  fading channels with pointing errors," *IEEE Internet of Things J.*, vol. 9, no. 14, pp. 11 772–11 783, 2022.
- [20] P. Bhardwaj, R. Khanna, and S. M. Zafaruddin, "A generalized statistical model for THz wireless channel with random atmospheric absorption," in *Proc. IEEE Wireless Commun. and Netw. Conf. (WCNC)*, 2024.
- [21] O. S. Badarneh and F. S. Almechadi, "On the sum of extended  $\eta$ - $\mu$  variates with MRC applications," *IEEE Commun. Lett.*, vol. 25, no. 11, pp. 3518–3522, 2021.
- [22] D. Dixit, P. Pandey, P. K. Verma, D. Sigroha, and D. K. Tripathi, "New exact ABER for MRC receiver in  $\kappa$ - $\mu$  faded channels," in *Proc. Int. Conf. IoT Commun. Autom. Technol. (ICICAT)*, 2023.
- [23] O. S. Badarneh, M. K. Alshawaqfeh, F. S. Almechadi, and H. S. Silva, "Selection combining over the extended  $\eta$ - $\mu$  fading channels," *IEEE Wireless Commun. Lett.*, vol. 11, no. 4, pp. 722–726, 2022.
- [24] F. J. Lopez-Martinez, J. F. Paris, and J. M. Romero-Jerez, "The  $\kappa$ - $\mu$  shadowed fading model with integer fading parameters," *IEEE Trans. Veh. Technol.*, vol. 66, no. 9, pp. 7653–7662, 2017.
- [25] T. M. Hoang, B. C. Nguyen, P. T. Tran, and L. T. Dung, "Outage analysis of RF energy harvesting cooperative communication systems over Nakagami- $m$  fading channels with integer and non-integer  $m$ ," *IEEE Trans. Veh. Technol.*, vol. 69, no. 3, pp. 2785–2801, 2020.
- [26] G. R. d. L. Tejerina, C. R. N. da Silva, R. A. A. de Souza, and M. D. Yacoub, "On the extended  $\eta$ - $\mu$  model: New results and applications to IRS-aided systems," *IEEE Trans. Veh. Technol.*, vol. 72, no. 4, pp. 4133–4142, 2023.
- [27] F. D. Almeida García, F. R. A. Parente, M. D. Yacoub, and J. C. S. S. Filho, "Exact  $\kappa$ - $\mu$  sum statistics," *IEEE Wireless Commun. Lett.*, vol. 12, no. 7, pp. 1284–1288, 2023.
- [28] —, "On the exact sum PDF and CDF of  $\alpha$ - $\mu$  variates," *IEEE Trans. Wireless Commun.*, vol. 22, no. 8, pp. 5084–5095, 2023.
- [29] M. Milisic, M. Hamza, and M. Hadzalic, "Outage performance of  $l$ -branch maximal-ratio combiner for generalized  $\kappa$ - $\mu$  fading," in *Proc. IEEE Veh. Technol. Conf. (VTC)*, 2008.
- [30] (2001) The Mathematical Functions Site. Wolfram Research, Inc. Accessed: Oct. 19, 2023. [Online]. Available: <http://functions.wolfram.com/>
- [31] G. R. d. L. Tejerina, C. R. N. da Silva, and M. D. Yacoub, "Extended  $\eta$ - $\mu$  fading models," *IEEE Trans. Wireless Commun.*, vol. 19, no. 12, pp. 8153–8164, 2020.
- [32] E. Kreyszig, *Advanced Engineering Mathematics*, 10th ed. Wiley Global Education, 2010.
- [33] I. S. Gradshteyn and I. M. Ryzhik, *Table of integrals, series, and products*, 7th ed. Elsevier/Academic Press, 2007.
- [34] M. D. Yacoub, "The  $\kappa$ - $\mu$  distribution and the  $\eta$ - $\mu$  distribution," *IEEE Trans. Antennas and Propag.*, vol. 49, no. 1, pp. 68–81, 2007.
- [35] M. K. Simon and M.-S. Alouini, *Digital communication over fading channels*. John Wiley & Sons, 2005.
- [36] "NIST Digital Library of Mathematical Functions," Version 1.2.3; Release date 2024-12-15. [Online]. Available: <https://dlmf.nist.gov/>
- [37] Y. Xing, O. Kanhere, S. Ju, and T. S. Rappaport, "Sub-terahertz wireless coverage analysis at 142 GHz in urban microcell," in *Proc. IEEE Int. Conf. Commun. (ICC)*, 2022.